J. Fluid Mech. (2008), *vol.* 596, *pp.* 221–260.
doi:10.1017/S002211200700955X Printed in the United Kingdom

Vortical structures and heat transfer in a round impinging jet

M. HADŽIABDIĆ† AND K. HANJALIĆ‡
Department of Multi-scale Physics, Delft University of Technology, Delft, The Netherlands

(Received 15 February 2007 and in revised form 1 October 2007)

In order to gain a better insight into flow, vortical and turbulence structure and their correlation with the local heat transfer in impinging flows, we performed large-eddy simulations (LES) of a round normally impinging jet issuing from a long pipe at Reynolds number $Re = 20\,000$ at the orifice-to-plate distance $H = 2D$, where D is the jet-nozzle diameter. This configuration was chosen to match previous experiments in which several phenomena have been detected, but the underlying physics remained obscure because of limitations in the measuring techniques applied. The instantaneous velocity and temperature fields, generated by the LES, revealed interesting time and spatial dynamics of the vorticity and eddy structures and their imprints on the target wall, characterized by tilting and breaking of the edge ring vortices before impingement, flapping, precessing, splitting and pairing of the stagnation point/line, local unsteady separation and flow reversal at the onset of radial jet spreading, streaks pairing and branching in the near-wall region of the radial jets, and others. The LES data provided also a basis for plausible explanations of some of the experimentally detected statistically-averaged flow features such as double peaks in the Nusselt number and the negative production of turbulence energy in the stagnation region. The simulations, performed with an in-house unstructured finite-volume code T-FlowS, using second-order-accuracy discretization schemes for space and time and the dynamic subgrid-scale stress/flux model for unresolved motion, showed large sensitivity of the results to the grid resolution especially in the wall vicinity, suggesting care must be taken in interpreting LES results in impinging flows.

1. Introduction

Impinging jets have been the subject of extensive research because of their widespread industrial application as efficient promoters of heat and mass-transfer rates. Consequently, most of the literature deals primarily with heat transfer and related bulk parameters of industrial relevance. More recently, it has been recognized that turbulent impinging jets, despite geometric simplicity, contain interesting physics, which makes them attractive for studying various features of turbulence dynamics, its interaction with the impinged wall and resulting effects on heat and mass transfer. Several recent publications focus on detailed experimental investigation of the

† Present address: International University of Sarajevo, Faculty of Engineering and Natural Sciences, Bosnia and Herzegovina.
‡ Present address: Dipartimento di Maccanica ed Aeronautica, University of Rome 'La Sapienza', Italy

flow and turbulence structure using laser diagnostics (laser-Doppler anemometry, LDA; particle image velocimetry, PIV; laser-induced fluorescence, LIF), liquid crystals, thermal tomography, and other techniques. Despite significant progress in understanding various phenomena in different configurations of a single or multiple impinging jets with different orifice shapes and orifice-to-plate distances, many issues remain open because of limitations in the available measuring techniques. Direct or large-eddy numerical simulations (DNS and LES), with their potential to provide the full four-dimensional (time and space) flow dynamics and to resolve all important turbulence scales, have thus been viewed as an inescapable route to providing comprehensive information and to complementing the experimental results.

The physical composition of impinging jets is not unique since it depends upon a number of parameters, such as the Reynolds number, nozzle-to-wall distance, inflow turbulence, jet configuration and orifice shape and profile. A common perception of a simple round impinging jet implies three distinct regions through which fluid passes – the free-jet, the stagnation zone and the radial wall-jet region, each featured by different prevailing turbulence dynamics and each governed by some specific generic turbulence mechanisms. One of the main processes that influence the jet dynamics and heat transfer is the growing unstable edge shear layer that surrounds the free jet core. The growth of the Kelvin–Helmholtz instabilities in the shear layer leads to the formation of roll-up vortices with a natural frequency characterized by the Strouhal number (St), defined in terms of jet-exit mean velocity W_b and nozzle diameter D, but the St value appeared also to be dependent on the nozzle-to-plate distance H. Periodic formation, coalescing and breakdown of the ring vortices lead to pressure pulsation in the jet irrespective of whether it is inviscid, or partially or fully turbulent (depending on the upstream turbulence intensity and nozzle shape), affecting significantly the heat transfer in the stagnation region. While these pulsations are present both in laminar and turbulent impinging jets, the character of the latter in the impingement region depends on the orifice-to-plate distance H/D. If the free-jet region is sufficiently long ($H/D > 6$, Livingood & Hrycak 1973), the jet core vanishes owing to the inward spreading of the edge shear layer. The existence of the jet core, especially if it is shear-free at the moment when the jet impacts the wall, has a profound effect on the Nusselt-number distribution, where the Nusselt number is defined as:

$$Nu = \frac{h_t D}{\lambda}, \tag{1.1}$$

where h_t is the heat transfer coefficient, D is the jet diameter and λ is the thermal conductivity.

In the developing zone, the axial velocity decays as a result of jet radial spreading owing to a strong shear at the jet boundary and the entrainment of the surrounding fluid, leading to a fully developed velocity profile. As the jet approaches the wall, the impermeability constraints begin to affect the velocity and stress fields. A stagnation region is formed in the centre of the impingement zone. The axial velocity diminishes fast, followed by a decrease of the axial momentum and the increase of the static pressure. Owing to the impermeability constraint, the jet deflects into the radial direction and a wall-jet is formed further downstream. Around the jet deflection region, corresponding to the maximum streamline curvature, the accelerating boundary layer becomes very thin, but it evolves soon into a radial wall-jet where the fluid is decelerated owing to radial spreading. The wall-jet is characterized by a strong shear with the turbulence level much higher than in an ordinary boundary layer.

Heat transfer, especially in the stagnation and jet deflection regions has been and still is surrounded by some controversy. Unlike in laminar regimes, where the Nusselt number usually shows a dip at the stagnation point, in turbulent jets the statistically averaged Nusselt number shows its maximum – unless the jet-exit-to-plate distance is very short and there is a potential jet core. Lee & Lee (2000) and Ashforth-Frost & Jambunathan (1996*b*), among others, found the maximum Nusselt number displaced from the geometrical jet centre in the same configuration and at a similar Reynolds number. Although not confirmed by the majority of reports (Baughn & Shimizu 1989; Lytle & Webb 1994; Yan & Saniei 1997; Geers, Hanjalić & Tummers 2006, among others), these findings add to the uncertainty and justify the present numerical studies. Because of relatively low turbulence intensity compared with the free-jet shear layer and the wall jet, and even negative production of kinetic energy detected by several experiments (Nishino *et al.* 1996; Geers, Hanjalić & Tummers 2004, 2006) and confirmed by the present numerical results, this *Nu* peak cannot be fully associated with stochastic turbulence. Major factors are the large-scale eddies formed from the broken ring vortices, which impinge periodically on the target plate. Kataoka (1990) argued that high heat transfer in the stagnation region is largely caused by the surface renewal effects of large-scale eddies. Their periodic impact on the target surface, together with the associated pressure pulsations, causes flapping and precessing of the jet core. Strong fluid acceleration and the consequent local thinning of the boundary layer somewhat away from the stagnation region (corresponding to the maximum streamline curvatures at the jet deflection) probably enhances heat transfer, but not directly in and around the stagnation point. The precise mechanism and the effects of different events depend much on the jet configuration, inflow turbulence level and structure, and the orifice-to-plate distance. According to Livingood & Hrycak, the maximum Nusselt number for a jet issuing from a nozzle without turbulence occurs for $H/D \approx 4$, whereas Nishino *et al.* and Baughn & Shimizu (in the latter, the jet issues from a fully developed pipe flow) found that the maximum *Nu* is achieved for $H/D = 5.8 - 6.0$. The optimum nozzle-to-plate distance apparently coincides with the length of the potential core, if it exists. As the velocity starts to decay beyond the potential core, the heat-transfer coefficient diminishes. For an initially turbulent jet (without a potential core), the optimum distance depends on the upstream turbulence and *Re* number.

Equally intriguing is the physics behind a second peak in the Nusselt number which appears in some situations, depending on the Reynolds number and nozzle-to-plate distance. Colucci & Viskanta (1996) attributed this second peak in the Nusselt number to transition from a laminar to a turbulent boundary layer in the wall-jet region, which appears reasonable if the incoming jet has a potential or a laminar core. Lytle & Webb (1991) and others associate the second peak with a high level of turbulent kinetic energy convected into the wall region from the edge jet shear layer. They reported that the location of the outer peak is highly sensitive to nozzle geometry, but also to the turbulence level in the issuing jet. Baughn & Shimizu (1989) measured the heat-transfer coefficient for impinging jets with different H/D and found that this parameter plays the major role in determining the distribution of the heat-transfer coefficient, concluding that the second maximum in the Nusselt number exists only for jets with $H/D < 6$. The main difference between jets with $H/D < 6$ and $H/D > 6$ is that in the latter case, the jet core disappears before the jet impacts the wall.

Other aspects have also been discussed in experimental studies (Livingood & Hrycak 1973; Baughn & Shimizu 1989; Kataoka 1990; Viskanta 1993; Nishino

et al. 1996) and others. The experiment of Cooper *et al.* (1993) provided detailed measurements of the mean-velocity and turbulence statistics for a single impinging jet issuing from a long pipe at $Re = 23\,000$ and $Re = 70\,000$. The experiment had well-defined inflow conditions (fully developed pipe flow), which makes it popular as a test flow for validating RANS turbulence models. The experiments of Nishino *et al.* (1996) provided important information about turbulence statistics in the stagnation region of an axisymmetric impinging jet. Geers *et al.* (2005, 2006) focused mainly on heat transfer in multiple impinging jets, but also provided some measurements and analysis of a single jet for the configuration identical to that of Baughn & Shimizu. Specific effects of the nozzle configurations have been investigated by Lee & Lee (2000), who found that different nozzle configurations not only change the heat-transfer rate, but also affect the shape of the Nusselt-number distribution in the wall-jet region. However, because of a large number of influential parameters and the difference in configurations and experimental conditions investigated, the comparison between different experimental and numerical results is difficult.

The existing numerical simulations (LES and DNS) of the impinging jets are limited to relatively low values of Reynolds number. Most reported LES studies deal with simpler plane (slot) jets, which feature somewhat different physics and pose less of a computational challenge than round jets (no radial spreading of the wall-jet). Voke & Gao (1998) reported on LES of a plane impinging jet at $Re = 6500$ focusing on the temperature variation on the plate surface, whereas Beaubert & Viazzo (2003) in their LES studied the influence of the Reynolds number and vortex dynamics in a similar plane geometry. Tsubokura *et al.* (2003) simulated in parallel both the plane and axisymmetric impinging jets, all externally excited, at $Re = 6000$ by LES and at $Re = 3000$ by DNS. They argued that the most important difference between the two jet types is in the stretching direction of the roll-up eddies coming from the shear layer. In the stagnation region of the plane jet they found distinct organized structures in the form of twin vortices, whereas in the round jet no organized structures were detected. Olsson & Fuchs (1998) have simulated a forced semiconfined round impinging jet with $H/D = 4$ and $Re = 10\,000$. Interactions of the large-scale structures and the wall-jet have been investigated in parallel with some numerical and modelling issues. One outcome was the detection of instantaneous periodic separation in the boundary layer in the wall-jet region, but it remains unclear if this phenomenon is pertinent only to externally excited jets because no data were presented for unexcited jets. Hattori & Nagano (2004) carried out a DNS of the turbulent heat transfer in a semiconfined plane impinging jet, focusing on the estimation of the averaged mechanism behind the second Nu peak. Based on the statistical budget of stress and heat flux components, the authors concluded that the turbulent diffusion of both the wall-normal heat flux and the turbulence intensity, their production and the pressure diffusion of the wall-normal turbulence intensity, all play important roles in the occurrence of the second peak of a local heat-transfer rate.

This brief review of the literature indicates that despite continuous efforts, the physics of the impinging jets is not fully understood. Experimental techniques are limited mainly to point- and plane measurements, and thus – apart from qualitative visualization using a passive tracer, remain short of providing comprehensive data in space and time, necessary to complete the physical picture. Especially critical is the region very close to the wall, which governs the wall heat-transfer. On the other hand, few results of computer simulations (DNS and LES) of impinging jets at higher Reynolds numbers can be found in literature, especially for round impinging jets. In several studies published, external forcing was imposed to create

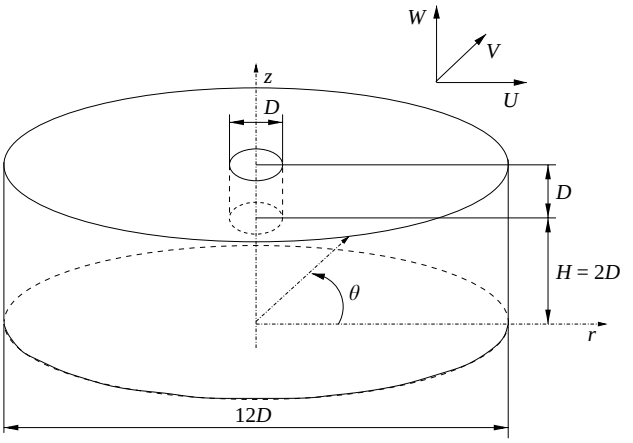

FIGURE 1. Schematic representation of the computed domain. The velocity components in the axial (z), radial (r) and azimuthal (θ) directions are denoted by W, U and V.

stronger coherent structures in order to maintain turbulence and to facilitate the simulations.

This paper reports on wall-resolved large-eddy simulations of a round jet issuing from a long pipe at $Re = W_b D/\nu = 20\,000$ with the orifice-to-plate distance $H/D = 2$, corresponding to the experimental configuration investigated by Baughn & Shimizu (1989), Cooper *et al.* (1993) and Geers *et al.* (2004, 2005). We opted for this configuration partly because several artefacts detected in these experiments call for further clarification. Moreover, because numerical simulation of impinging flows at higher Re numbers proved to be highly sensitive to the computational grid and the subgrid-scale model, prior to their use to extract information on flow physics it is highly recommended that the credibility of the simulations be validated with the available experimental results. The paper begins with the specification of the flow configuration, discussion of inflow and boundary conditions, computational grid, the subgrid-scale model and numerical approach used. Section 3 presents selected statistically averaged mean flow and turbulence properties and an analysis of grid resolution. The main outcome of the study focusing on the impinging jet structure is presented in § 4, where the vorticity and coherent-eddies dynamics in each of the three characteristic flow regions are discussed. Section 5 considers the temperature and heat transfer. We give additional consideration to the correlation between the velocity and temperature fields, followed by conclusions in § 6.

2. Flow configuration and computational method

2.1. *Solution domain and computational grid*

Large-eddy simulations were performed with the in-house unstructured finite-volume computational code TFlowS, with the cell-centred collocated grid structure (Ničeno 2001; Ničeno & Hanjalić 2004). More details about the code application to impinging flows can be found in Hadžiabdić (2006).

A circular jet issuing from a fully developed pipe flow, enters a cylindrical solution domain with a diameter of $12D$ and a height of $3D$, and impinges on the target plate located $2D$ from the pipe exit (figure 1). Designing a rational grid which will meet the strict resolution requirements in the near-wall region in such a domain, and yet be

Grid Number	Azimuthal domain (deg.)	Number of processors	Number of grid cells N_z	N_r	N_θ	Total
Grid I	360°	48	68	168	1080	9.4×10^6
Grid II	360°	48	154	168	504	9.9×10^6
Grid III	90°	48	154	180	200	4.9×10^6
Grid IV	360°	48	80	168	300	7.5×10^6

TABLE 1. Grid features.

manageable with the available computing facilities, required a significant effort and a trial-and-error procedure, because *a priori* meshing criteria for such a flow, especially at higher *Re* numbers, are not available.

Four different computational grids were considered (table 1), all of the hybrid type with triangular prisms in the region $r/D < 0.5$ and hexahedral cells in the rest of the domain. A similar hybrid mesh used in the pipe flow shows satisfactory results, as shown in the Appendix. The wall-nearest value of z^+ at the impingement plate was smaller than 1.0 for all grids.

Grid I. Grid I consisted of 9.4×10^6 cells, where the majority of the cells were concentrated in the impingement region. The mesh was hyperbolically clustered towards the impingement wall in such a way that the centre of the first grid node was at $z/D = 4.6 \times 10^{-4}$. The increment in the cell thickness was never larger than 15 % and for most of the cells was smaller than 7 %. For the Reynolds number considered, this distance corresponds to $z^+ \approx 1$ for the maximum friction velocity that occurs at $r/D \approx 1.0$. Figure 2 shows the dimensionless spacing in the radial and azimuthal directions at several locations. The wall surface area increases rapidly with an increase of the radial coordinate and it is difficult to avoid high-aspect-ratio cells near the wall without a prohibitive increase in the number of the total grid points. However, in the area of interest ($r/D < 3.0$) the mesh resolution is close to the generally accepted LES criteria for wall-attached flows estimated by Piomelli & Chasnov (1996) which requires that $\Delta r^+ < 100$, $(r\Delta\theta)^+ < 20$ and $\Delta z^+ < 2$. Although fulfilling these criteria ensures satisfactory results for channel and pipe flows, it is less certain that the same mesh resolution (especially in the radial direction) is sufficiently high to resolve the small-scale streaky motion in the area of strong acceleration or deceleration of the flow.

The mesh resolution quality can also be estimated by comparing the mesh size $\Delta = [\Delta r \times r\Delta\theta \times \Delta z]^{1/3}$ to the Kolmogorov length scale $\eta = (\nu^3/\varepsilon)^{1/4}$ where ν is the molecular viscosity and ε is the dissipation rate estimated from the prior RANS solution using the $\zeta - f$ model (Hanjalić, Popovac & Hadžiabdić 2004). For isotropic turbulence, Pope (2000) among others, showed that a grid spacing of 12η is required in order to resolve the major contributions to the dissipation. Figure 3 shows the discretization levels achieved by the different grids. For Grid I, the ratio $\Delta/\eta < 12$ for the part of the domain where $r/D < 2$ while at the station $r/D = 2$ the ratio $\Delta/\eta \approx 16$.

The number of cells in the axial (z) and radial (r) directions was 68 and 168, respectively, while the azimuthal (θ) direction was meshed with 1080 cells for $r/D > 0.5$. The velocity-field data recorded from the LES simulation of the pipe flow were copied to the jet entrance located at $z/D = 2.0$. The thickness of the pipe wall was assumed to be infinitesimally thin. From $z/D = 2.0$ to $z/D = 0.5$, the mesh in the axial direction was uniformly distributed. The mesh was divided into 48 equally

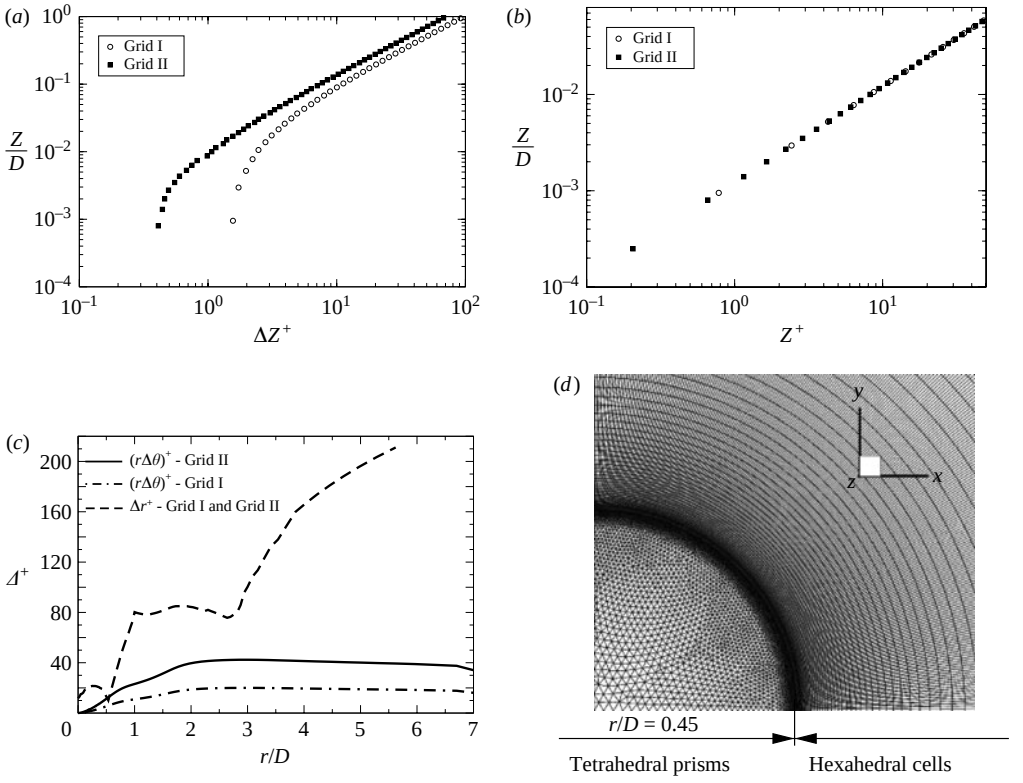

FIGURE 2. (*a*) Dimensionless spacing in the axial direction at the position $r/D = 2$. (*b*) Mesh resolution in the axial direction $r/D = 2$. (*c*) Dimensionless spacing in the radial and azimuthal directions. (*d*) Top view of a mesh segment of Grid I.

grid balanced sub-domains. Each sub-domain was saved to a separate file as an independent identity.

Grid II. Grid II differed from Grid I in the mesh distribution in the azimuthal and axial directions, while the distribution of the grid points in the radial direction remained approximately the same. This grid was designed to diminish the deficiencies of Grid I, mainly the insufficient mesh resolution at the jet-entrance region. This deficiency resulted in an overestimation of the turbulent kinetic energy in the mixing region. Grid II contained 154 cells in the axial direction with a strong hyperbolic clustering at both ends. The first computational cell at the jet entrance had a value of $\Delta z/D = 0.002$ compared to $\Delta z/D = 0.03$ in Grid I. In order to keep the total grid size within acceptable limits (up to 10 million cells, dictated primarily by the local computing facilities used for data post-processing), the number of cells in the azimuthal direction was decreased by a factor of two ($N_\theta = 504$). The total number of cells was 9.9 million. The mesh was divided in the same number of sub-domains (48). The dimensionless spacing in the radial and axial directions are shown in figure 2. The resolution in the azimuthal direction diminished from $(r\Delta\theta)^+_{max} = 20$ (Grid I) to $(r\Delta\theta)^+_{max} = 40$, but the mesh resolution in the axial direction became significantly better, see figure 2(*a*). Figure 3 shows that the ratio Δ/η decreases significantly in the jet shear-layer region, compared to Grid I. However, the mesh resolution becomes

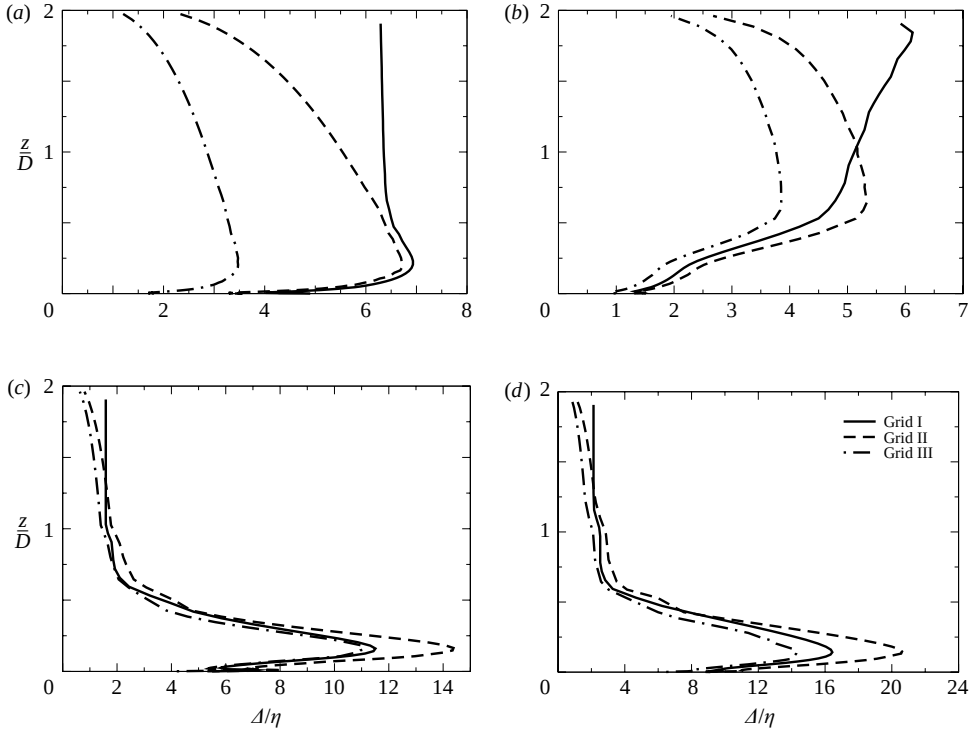

FIGURE 3. Estimated ratio Δ/η at different radial positions: (*a*) $r/D=0$; (*b*) $r/D=0.5$; (*c*) $r/D=1.0$; (*d*) $r/D=2.0$.

coarser in the wall-jet region and Δ/η exceeds 12 owing to the smaller number of cells in the azimuthal direction ($\Delta/\eta=14$ in $r/D=1.0$ and $\Delta/\eta=21$ in $r/D=2.0$).

Grid III. The only way to significantly improve the mesh resolution within the available limits was to reduce the solution domain. For further testing of the mesh resolution, we considered a quarter of the full three-dimensional domain, i.e a 90° segment meshed with a new grid with the total number of cells of about 5 million, thus corresponding to 20 million points for the full cylindrical three-dimensional domain. Since the numerical code used does not support the periodic conditions (except for the orthogonal mesh) at the sides of the solution segment, we applied symmetry conditions. Because such conditions are not physically justified, especially when coherent ring structures are present, small segments of the solution domain (around 10°) next to each boundary were excluded from statistics. It is thus assumed that the major part of the solution domain used for the flow analysis and gathering the statistics, was unaffected by the boundary condition. Grid III contained 154 cells in the axial direction, 200 cells in the azimuthal direction (which corresponds to 800 cells for a full perimeter) and 180 cells in the radial direction. An improvement in the mesh resolution can be seen in figure 3. The ratio Δ/η is smaller than 12 for all plotted positions except $r/D=2.0$ where $\Delta/\eta=14$. As in the previous cases, the mesh was divided into the same number of sub-domains (48).

Grid IV. In all the above described meshes, the jet inflow was located at $z/D=2$. This, together with the assumption of an indefinitely thin pipe wall, was the major difference in the computed jet configuration compared with that used in the experiments. Grid IV was created in order to study the possible influence of

these differences. The inflow boundary condition is imposed at the pipe cross-section $1D$ upstream from the pipe exit, and the pipe wall was assumed to have the same thickness as in the experiment, $0.1D$. This configuration allowed the flow to adjust to the pipe exit. The number of points in the axial direction was 80, while in the region $r/D > 0.5$, the number of points in the azimuthal direction was 300. The radial spacing was similar to that in Grid II.

The simulations on four different high-density grids required a large computational effort and in order to rationalize, an interpolation algorithm was developed which made it possible to interpolate the results obtained on one mesh to the other, which saved a significant amount of computational time. Nevertheless, the computational costs still remained excessive: the averaged cost per simulation per mesh on the National Teras Supercomputer was 40 000 CPU.

2.2. *Boundary and inflow conditions*

Apart from the impinged wall, for which no-slip conditions were imposed for velocity, and a constant heat flux was specified as in the experiment, the definition of the boundary conditions for such an open domain is not straightforward. For the outflow boundaries, we applied a convective boundary condition defined by the hyperbolic convective equation, (2.1), which allows fluid to leave the computational domain with only a small perturbation of the flow in its interior:

$$\frac{\partial U}{\partial t} + C_{vel}\frac{\partial U}{\partial r} = 0, \tag{2.1}$$

where C_{vel} is the mean convective velocity and U is the radial component of the velocity vector. The convective velocity was estimated at each time step from the mass balance:

$$\int_{S_{inflow}} W \mathrm{d}S = \int_{S_{outflow}} C_{vel} \mathrm{d}S. \tag{2.2}$$

As reported by Pauley, Moin & Reynolds (1990), we also found that flow in the jet area is not very sensitive to the values of the convective velocity. The same boundary condition was used for the energy equation at the outlet boundary.

The inflow conditions in LES pose a challenge because a large part of the velocity spectrum ought to be specified at each time step. Imposing the mean flow with random perturbations was generally not successful (Fröhlich & Rodi 2002) since these perturbations are not physical and produce erroneous turbulence statistics. In order to match the inflow condition used in the reference experiments, the jet inflow is generated by a separate LES simulation of the fully developed turbulent pipe flow. The velocity field in the pipe exit plane was recorded and stored at every time step. These data were subsequently used to define the inflow velocity components for the jet simulation. The results of the pipe flow simulation were in good agreement with the available DNS data as shown in the Appendix.

Still less obvious was the choice of the boundary condition at the top free boundary at $z/D = 3$. The reference experiments had an open boundary which allowed entrainment of the surrounding flow into the jet region. The influence of this boundary condition on the flow and turbulence in the jet region was difficult to estimate. The RANS computations had shown no influence on the velocity field and heat transfer in the whole jet (Behnia *et al.* 1999). Ashforth-Frost & Jambunathan (1996*a*) investigated the effect of semi-confinement on the jet flow fields and stagnation-point heat transfer experimentally. They found that semi-confinement causes more significant differences in the turbulence intensity and heat transfer (15 % difference in the absolute level of

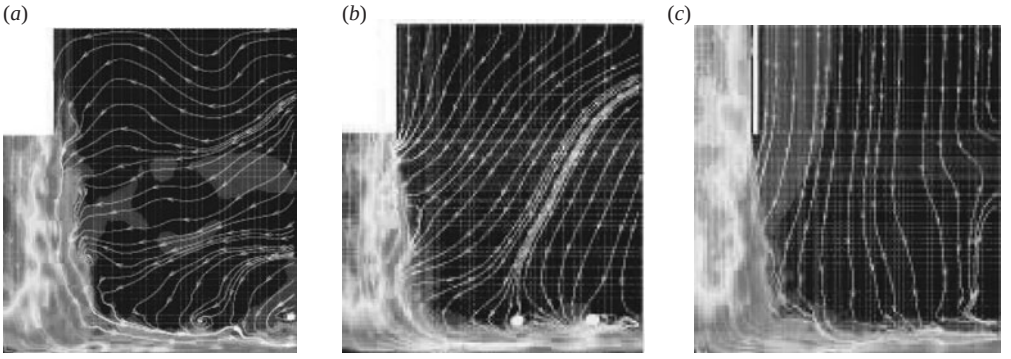

FIGURE 4. Instantaneous velocity-magnitude fields and the corresponding streamlines obtained with different boundary conditions on the top boundary: (*a*) convective outflow on Grid I; (*b*) constant inflow of $-0.01W_b$ on Grid II; and (*c*) pressure boundary on Grid IV.

turbulence intensity and 10 % for the stagnation point heat transfer) at the position $z/D \approx 5$ while at stations $z/D = 1.5$ and $z/D = 2$ the differences appeared to be much smaller (the difference in the mean velocities is less than 1 %). In order to minimize the influence of the top boundary, we displaced it $1D$ above the jet entrance. In such a way, we diminished the effect of the top boundary condition that might influence the turbulence field and heat transfer rate in the region of interest.

In order to investigate the influence of the top boundary condition on the flow simulations, three different conditions have been considered: the convective-, the inflow- and the pressure-type boundary conditions.

The *convective* outflow produced a flow pattern similar to that obtained in the semi-confined jet configuration (with a solid wall instead of a free boundary at the top) reported by Behnia *et al.* (1999) using RANS. The flow entered the domain in the upper part of the outlet boundary and moved towards the jet region. The convective outflow condition is designed for the outlet boundary on which the velocity component perpendicular to the outlet plane is dominant. Since it was not clear how to estimate the convective velocity, a constant value of C_{vel} has been adopted ($C_{vel}/W_b = -0.01$). The mass flux throughout the top boundary was insignificant.

The *inflow* boundary condition imposes a constant velocity vector perpendicular to the top free plane and directed towards the impingement plate. The magnitude of the inlet velocity vector was 1 % of the jet bulk velocity. With these conditions, the flow migrates slowly from the top boundary towards the jet region.

The *pressure* boundary condition allowed the flow to pass out of or into the domain, depending on the local pressure values. The resulting flow pattern was similar to the one with the inflow boundary. The pressure boundary condition produced a similar mass flux throughout the top boundary with a maximum inlet velocity of 3 % of the jet bulk velocity.

However, despite a large difference in the streamline patterns (figure 4), as in the RANS computations, no significant differences in the results within the jet itself were noticed for different top boundary conditions. Closer examination revealed that the velocity in the domain outside the jet is very small compared to those in the jet.

On the other hand, the jet edge shear layer acts as a shear shield, preventing, or at least diminishing, any effect of the outer motion. The difference in the maximum mean velocity in the wall-jet region for three different top boundary conditions is

less than 1 %. The difference in the mass flux, obtained by integrating velocity over a cylindrical surface at $r/D = 1.0$ is less than 4 %. If the integration is confined to $Z/D < 1.0$ (the region of interest), the difference is only 0.7 %. Hence, irrespective of the boundary conditions at the top boundary and very different streamline patterns, the results for the jet were little affected.

2.3. *Subgrid-scale model and discretization*

The large-eddy simulations presented here have been performed by solving the standard form of the filtered Navier–Stokes and continuity equations for incompressible fluid, closed with the Smagorinsky dynamic subgrid-scale model (SGS) of Germano *et al.* (1991). The subgrid-scale eddy viscosity is defined as:

$$\nu_t = (C_s l_s)^2 |\overline{S}|, \tag{2.3}$$

where $|\overline{S}| = \sqrt{2\overline{S_{ij}}\ \overline{S_{ij}}}$ is the magnitude of the strain rate $\overline{S_{ij}}$, l_s is the length scale of the unresolved motion determined by the characteristic mesh size ($l_s = (\Delta V)^{1/3}$) and C_s is the Smagorinsky constant determined by the dynamic procedure proposed by Germano *et al.* (1991). The eddy viscosity was bound to zero by clipping, that sets $(C_s l_s)^2$ to zero when the SGS viscosity is negative.

Other SGS models, primarily the classic Smagorinsky subgrid model with a fixed constant, have also been tested. However, in order to eliminate any influence of the SGS model and *a priori* defined Smagorinsky constant (which is not uniquely defined in complex flows such as impinging jet), we confined our discussion to the results obtained with the dynamic model.

The central-difference scheme was used to discretize diffusive and convective terms in the momentum equations. However, some numerical instabilities were detected in the form of oscillatory wiggles in the velocity field in the small ring region very close to the wall at $r/D \approx 0.45$. The problem was cured by applying the second-order accurate upwind-biased scheme QUICK (Leonard 1979, 1988) locally in the thin circular region within $r/D < 0.5$ and $z/D < 0.15$.

The probable cause of the numerical instabilities can be attributed to two sources. First, this region is characterized by a strong radial flow acceleration, which is known to be sensitive to the central differencing discretization of the convective term. However, a more probable cause of instability is related to the shape of grid cells: it is indicative that the oscillations were observed only in the region meshed with the triangular prisms. In contrast to the hexahedral cells, the triangular ones have only three neighbouring cells in the horizontal plane with sharp angles between the side planes, which worsens the accuracy of the computation of the velocity gradients and can lead to numerical oscillations. This can be prevented either by refining the mesh in the affected region, or by applying a more diffusive numerical scheme. Since the affected region is characterized by high pressure gradient, it is not likely that the numerical diffusion associated with the QUICK scheme significantly affects the overall accuracy. The discretization of the energy equation was similar to that for the momentum equations, except that the QUICK convective scheme was used throughout to avoid overshoot which can otherwise lead to the occurrence of negative temperatures.

Time-marching was performed using a fully-implicit three-level time scheme. The time step was set to $\Delta t W_b/D = 0.0005$ and was kept constant during the simulation. Only in isolated regions with high velocities, did the CFL number reach 1, whereas in most other areas, the typical value was around 0.5. The iterative pressure correction algorithm (SIMPLE) was used for coupling velocity and pressure.

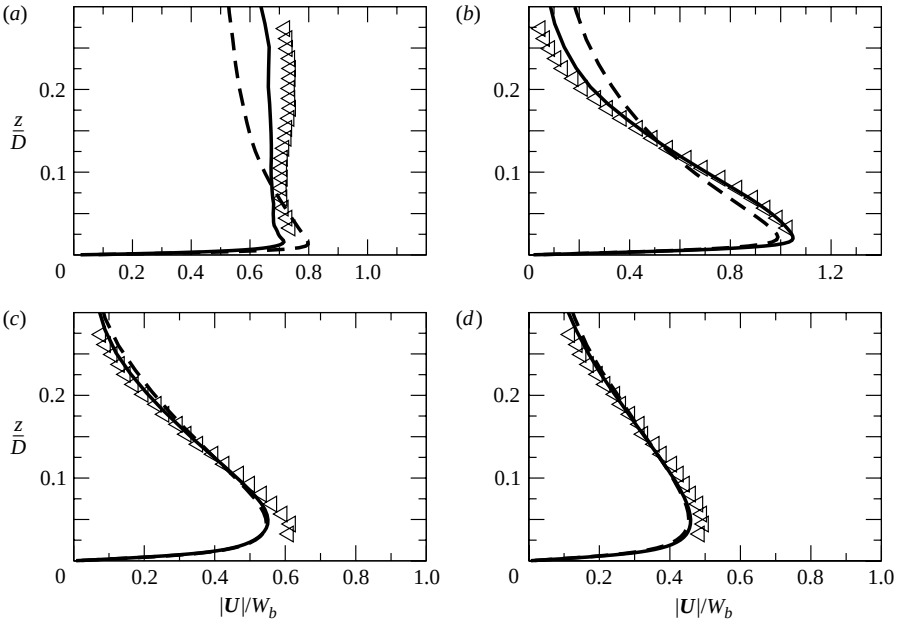

FIGURE 5. Comparison of mean-velocity profiles in the near-wall region at different radial locations obtained with ---, Grid I and ——, Grid II. Δ, Cooper *et al.* (1993). (*a*) $r = 0.5$, (*b*) 1.0, (*c*) 2.5, (*d*) 3.0.

The collection of results for the turbulence statistics started after 8 cycles and continued over a period of 16 cycles (with the cycle period evaluated from the estimated $St = 0.64$)

3. Mean flow properties and turbulence statistics

We present first a selection of time-averaged results for the velocity and turbulent stress fields and discuss some general flow features. The results obtained with different grids are compared with the available experimental data in order to validate the meshing quality and to establish sufficient credibility in the adopted LES strategy.

3.1. *Experimental validation and effect of mesh density*

There is no purpose in showing results obtained with all four grids, since some of the grids tested appeared to be inadequate. Despite careful consideration, designing in advance a grid that would provide sufficient resolution in all flow domains, and yet be rational and manageable with reasonable computer resources, appeared to be quite a challenge. This point is illustrated by figure 5 which shows profiles of the velocity modulus at different radial planes for Grids I and II. Despite the fact that Grids I and II have almost the same total number of cells and a similar grid structure, the different resolution in the axial and azimuthal directions (table 1) leads to a large difference already in the mean velocity, which is usually more robust to the grid resolution than the second and higher moments. The results for Grid I at $r/D = 0.5$ and 1 are far from satisfactory, despite the fact that the near-wall spacings in this grid satisfy all *a priori* near-wall resolution criteria ($\Delta z_1^+ \approx 1$, $r\Delta\theta_1^+ < 20$). Moreover, the subgrid-scale eddy viscosity ν_t/ν (figure 6) is smaller in the near-wall area, than in

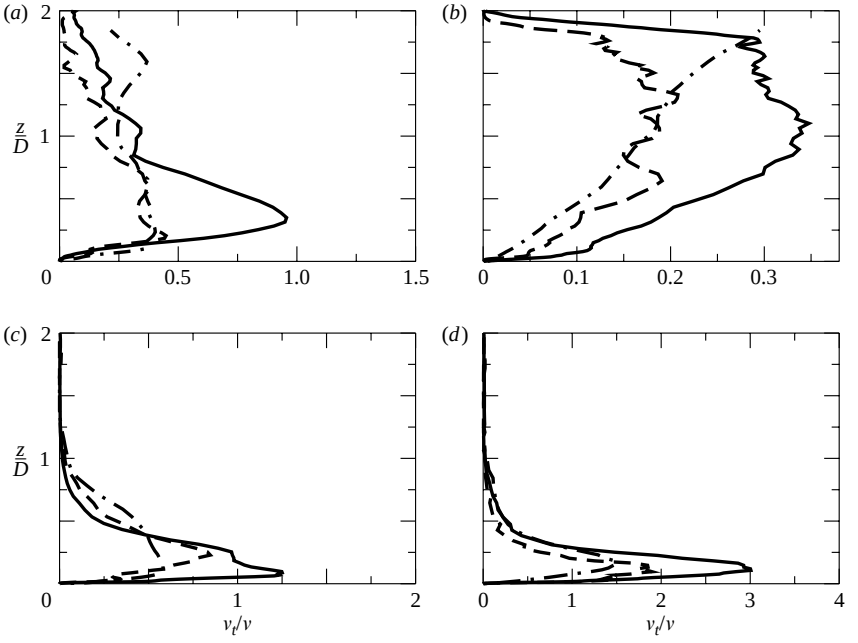

FIGURE 6. Distribution of subgrid-scale eddy viscosity at different r/D positions obtained with •—•, Grid I; ——, Grid II and - - -, Grid III. (*a*) $r/D = 0$, (*b*) 0.5m (*c*) 1.0, (*d*) 2.0.

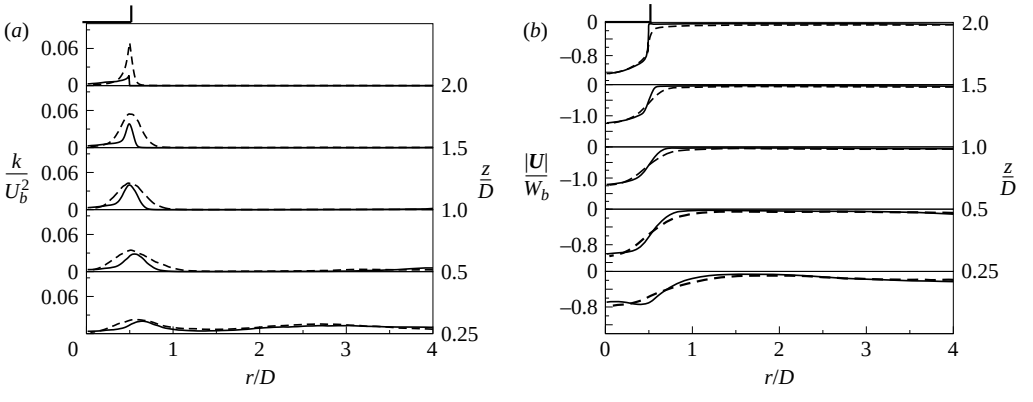

FIGURE 7. (*a*) Profiles of the turbulent kinetic energy and (*b*) of the velocity magnitudes at different z/D positions obtained with - - -, Grid I and ——, Grid II.

other grids considered. Nevertheless, poor agreement in figure 5 shows obviously that Grid I is poorly designed. In order to obtain a sufficiently fine mesh resolution in the impingement region, the large majority of grid cells were clustered in the zone below $z/D = 1.0$. However, it appeared that the pipe exit was meshed with far fewer cells than were needed to resolve accurately the development of the initial jet shear layer. As a result of the poor mesh resolution, the turbulent kinetic energy in the initial shear layer was dramatically overpredicted (figure 7*a*) causing a strong mixing and a faster propagation of the shear layer and its instabilities from the periphery towards the jet

centre. This is illustrated by figure 7(*b*), in which the velocity profiles from Grids I and II are compared in the wall-parallel planes at several locations. The velocity profiles from Grid I are smoother at the jet edge owing to a high kinetic energy in the region. The erroneous turbulent kinetic energy from the initial shear layer is convected downstream, thus affecting the predictive quality in the impingement and wall-jet regions (figure 5). The resulting Nusselt number from Grid I had a maximum value at the stagnation point, after which it gradually decreased without a second peak (see figure 29). It resembled the Nusselt-number profiles for those jets whose nozzle-to-plate-distance ratio is higher than $z/D = 4$. This means that the erroneous Nusselt number is due to a too strongly mixed jet core, caused by unphysically large turbulent kinetic energy in the jet shear layer.

As discussed in § 2.1, Grid II was designed in order to improve the deficiencies of Grid I. The number of cells in the axial direction was 2.3 times higher than in Grid I. The improved mesh resolution in the jet-entrance region made it possible to accurately predict the growth of the turbulent kinetic energy in the initial jet shear layer. This appeared to be a key prerequisite for accurate prediction of the turbulence level in the stagnation- and wall-jet regions, as shown in the improved distribution of the Nusselt number (figure 29). Far from the jet centre, for $r/D > 2$, however, the Nusselt number from both grids is underpredicted. This is probably caused by a deterioration of the mesh resolution owing to the radial spreading of the wall-jet.

Grid III meshed only a quarter of the three-dimensional domain allowing us to double the grid density and thus increasing the mesh resolution in all directions while still complying with the limit on the available computer memory. The resulting mean-velocity field did not differ significantly from that obtained on Grid II. However, despite the inconsistency in using symmetry instead of periodic boundary conditions, the predictions of the Nusselt number showed the expected improvements, especially in capturing the second *Nu* peak (figure 29), indicating that the time-averaged symmetry is preserved and thus the instantaneous lack of symmetry did not produce much effect on the time-mean wall parameters. The finer mesh resolution in the radial direction is considered to contribute most to the improvement.

With Grid IV, an attempt was made to account for the pipe wall thickness and to resolve better the pipe exit region. Inserting more cells around the pipe exit required, however, a significant additional decrease in the number of cells in the azimuthal direction, making the azimuthal resolution worse with cells size as large as $(r\Delta\theta)^+ = 68$ in some parts of the impingement region. The resulting Nusselt number had a larger error than that obtained on Grids II and III. Despite the more realistic jet configuration (compared to the experimental configuration), the error caused by a very coarse mesh resolution in the azimuthal direction neutralized possible improvements. Because of a poor mesh resolution of Grid IV in the azimuthal direction, no definite conclusion on the influence of the jet inlet could be drawn.

The influence of the mesh density on the subgrid-scale eddy viscosity level can be compared in figure 6. Grid II generated higher eddy viscosity than Grids I or III in most of the flow regions. However, Grid I produced a higher eddy viscosity especially in the region close to the nozzle exit owing to the poor local mesh resolution. The full scale of the failure of Grid I to resolve the flow in the nozzle-exit region cannot be detected by ν_t because the length scale used ($\Delta = (\Delta\ V)^{1/3}$) does not contain information about the cell anisotropy.

In the next section, we show only results obtained with Grid II.

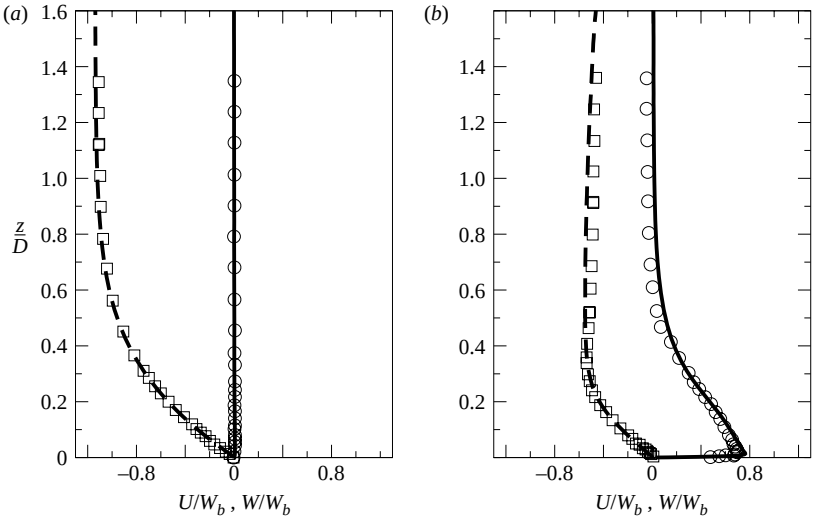

FIGURE 8. Mean radial and axial velocity profiles at (*a*) $r/D = 0$, and (*b*) $r/D = 0.5$; symbols, experiments of Geers (2004). - - -, WW_b; ——, U/W_b.

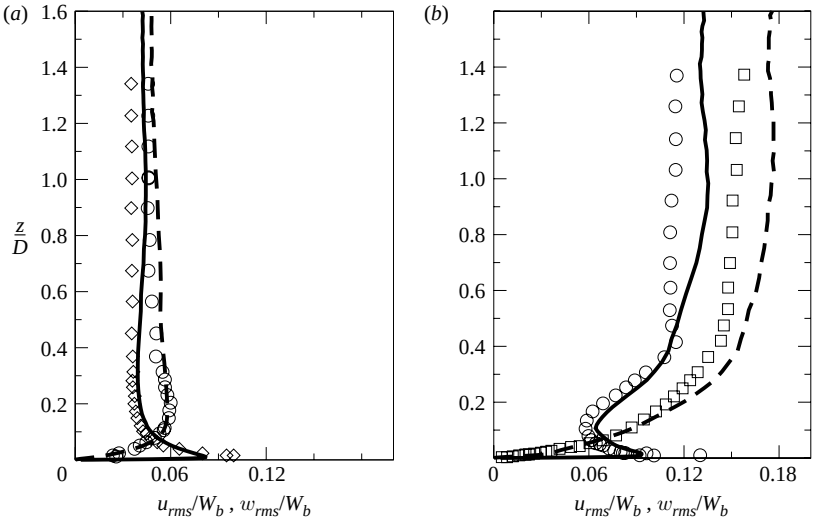

FIGURE 9. Root mean square of radial and axial velocities at (*a*) $r/D = 0$, and (*b*) $r/D = 0.5$; symbols, experiments of Geers (2004). ——, u_{rms}/W_b; - - -, w_{rms}/W_b.

3.2. *Velocity and turbulence energy*

Figures 8(*a*) and 9(*a*) show the axial and radial mean-velocity components and the r.m.s. of their fluctuations at the station $r/D = 0$, in excellent agreement with the experiments of Geers *et al.* (2006). On the centreline, the mean-axial velocity ($\overline{W}$) remains nearly constant for $z/D > 1.0$. Below $z/D = 1.0$, the flow decelerates owing to the presence of the impingement wall. An indication that the jet core is longer than the distance between the nozzle and the impingement wall are the constant values of the turbulence intensities u_{rms} and w_{rms} on the centreline down to $z/D = 0.3$ (figure 9*a*). This is consistent with the findings of Cooper *et al.* (1993) and Kataoka

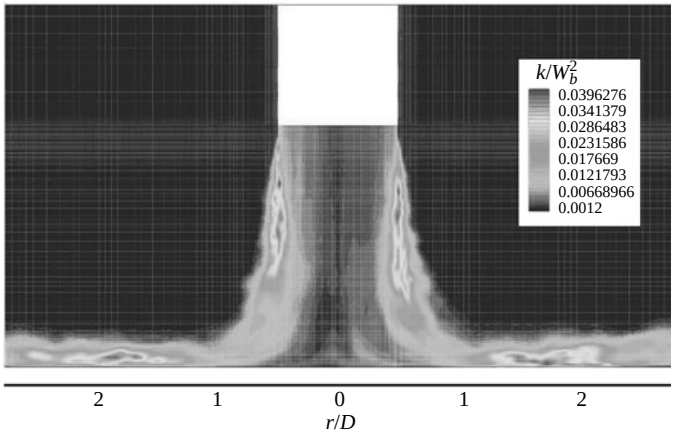

FIGURE 10. Contours of the turbulence kinetic energy.

(1990), who found that the jet core extends up to 4 to 6 nozzle diameters for turbulent jets.

Figures 8(*b*) and 9(*b*) show the mean velocities and the corresponding r.m.s. values of the radial- and axial-velocity components at the position $r/D = 0.5$. This position approximately coincides with the centre of the jet shear layer. As a result, the velocity fluctuations at this position are much stronger than in the central region of the jet. The strong anisotropy of turbulence is indicated by the difference between the r.m.s. values of the radial- and axial-velocity fluctuations.

Below the position $z/D = 0.5$, the wall presence causes a strong flow deflection. The radial velocity begins to increase and reaches its maximum at the edge of a newly formed boundary layer, while the axial velocity approaches zero at the wall. The velocity fluctuations also start to decrease owing to the wall-blocking effect. However, the r.m.s. value of the radial velocity increases again in the near-wall region owing to the growth of turbulence production caused by the near-wall shear. The turbulent stress field at the position $r/D = 0.5$ shows a strong anisotropy in the near-wall region, just as observed at $r/D = 0$. While the mean-velocity components at the station $r/D = 0.5$ agree well with the experimental data of Geers *et al.*, the r.m.s. values of the axial and radial velocity fluctuations predicted by LES in the region $z/D > 0.4$ are higher than measured, by roughly 17 % for the radial component and 12 % for the axial component.

The differences are attributed to possible small mismatching of the LES configuration and inflow conditions from the experiments. Even though the general mesh criteria are satisfied in this region, the apparent differences in the turbulent stress fields could also be mesh related.

We now move on to discuss in more detail the turbulence kinetic energy $k = \overline{u_i u_i}/2$ and its statistical production, especially in the stagnation region. A snapshot of the turbulent kinetic energy field (figure 10) reveals that its main production (as well as of all components of the turbulent stress tensor $\overline{u_i u_j}$) takes place in the high-shear regions, initially in the jet-edge shear layer, and further downstream in the wall jet. The maximum k occurs in the shear layer roughly half-way downstream from the jet exit, then decays in the highly curved jet deflection region, and recovers again in the wall jet where its maximum value exceeds that in the shear layer. In the jet core, however, there is not much activity.

Recall that the jet issues from a long pipe, thus possessing all the flow and turbulence features of a fully developed pipe flow with a kinetic energy peak close to the jet edge. Figure 7 (solid line, Grid II) shows quantitatively the evolution of k, with its peak in the jet-edge shear layer increasing as the jet develops. From the pipe exit at $z/D = 2.0$ to $z/D \approx 1.5$, the peak k doubled and continued to rise until $z/D \approx 1$ when it reaches its maximum. After this, k begins to decrease owing to a stronger lateral diffusion, but primarily because of radial spreading of the mixing layer, caused by the blockage of the impermeable wall. This decay in k is accompanied by a decrease and smoothing of the velocity gradient at the jet periphery. However, the mean velocity in the jet centre remains unchanged up to $z/D = 0.5$.

It is noted that the turbulence kinetic energy in the stagnation region remained relatively small, roughly at the level or even smaller than the inflow turbulence at the pipe axis. Since the Nusselt number reaches its maximum precisely at the stagnation point, this finding suggests that turbulence plays here only a minor role in the intensification of heat transfer. Nevertheless, the turbulence dynamics in the stagnation region warrants a closer examination. This region is characterized by high values of the static pressure and strong curvature of streamlines caused by the wall acting as an obstacle. As seen from the axial momentum equation on the jet centreline,

$$\overline{W}\frac{\partial \overline{W}}{\partial z} + \frac{1}{r}\frac{\partial r\overline{uw}}{\partial z} + \frac{\partial \overline{ww}}{\partial z} + \frac{1}{\rho}\frac{\partial \overline{p}}{\partial z} = 0, \tag{3.1}$$

where r and z are the radial and axial coordinates, and $\overline{U}$ and $\overline{W}$ are radial and axial velocity components, respectively, the static pressure increases along the central streamline at the expense of the axial momentum $\overline{W}(\partial \overline{W}/\partial z)$ and of the axial turbulent normal stress $\partial \overline{ww}/\partial z$ (with $\overline{uw} = 0$ along the centreline), because both $\overline{W}$ and $\overline{ww}$ decrease as the wall is approached. The latter shows that close to the wall, the momentum is transported back from fluctuations into the mean-velocity field, indicating also a reverse transfer of energy. The LDA measurements by Geers *et al.* for $H/D = 2$ and the PIV data by Nishino *et al.* (1996) for $H/D = 5.86$ both showed that the negative production of turbulent kinetic energy occurs for $z/D < 0.1$. Since the measurements with any technique very close to a solid wall are difficult and associated with uncertainties, we analysed the production of kinetic energy P_k using the present wall-resolved LES. In cylindrical coordinates, P_k is defined as:

$$P_k = -\overline{uu}\frac{\partial \overline{U}}{\partial r} - \overline{uw}\frac{\partial \overline{U}}{\partial z} - \overline{uw}\frac{\partial \overline{W}}{\partial r} - \overline{ww}\frac{\partial \overline{W}}{\partial z} - \overline{vv}\frac{\overline{U}}{r}. \tag{3.2}$$

By focusing only on the axis of symmetry and applying the axisymmetric conditions (combined with the continuity equation)

$$\overline{uu} = \overline{vv}, \quad \frac{\partial \overline{U}}{\partial r} = \frac{\overline{U}}{r}, \quad \frac{\partial \overline{W}}{\partial r} = 0, \quad \frac{\partial \overline{W}}{\partial z} = -\frac{\partial \overline{U}}{\partial r} - \frac{\overline{U}}{r}. \tag{3.3}$$

(3.2) can be simplified to

$$P_k = 2(\overline{ww} - \overline{uu})\frac{\partial \overline{U}}{\partial r}. \tag{3.4}$$

The production of turbulent kinetic energy is proportional to the difference of the turbulent normal stresses on the axis of symmetry. The value of $\overline{ww}$ decreases monotonically towards zero while $\overline{uu}$ has a peak in the wall vicinity and then sharply decreases to zero at the wall (figure 12*b*). A significant difference in the axial and radial velocity fluctuations reveals a strong anisotropy. The value of $\partial \overline{W}/\partial z$ is negative

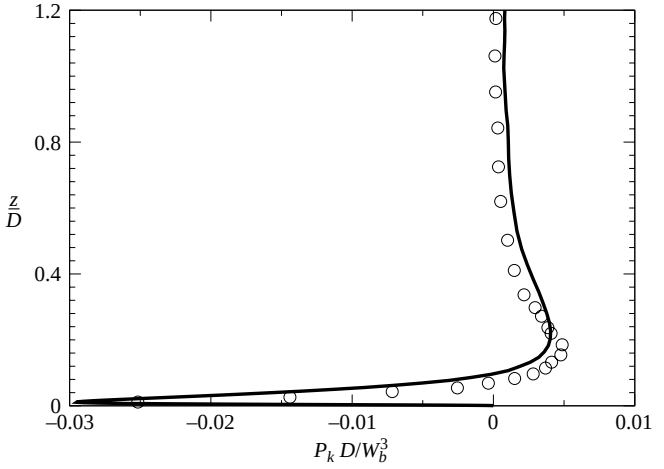

FIGURE 11. ——, Profile of the turbulence kinetic energy production along the centreline of the jet compared with ○, the experimental data of Geers *et al.* (2004).

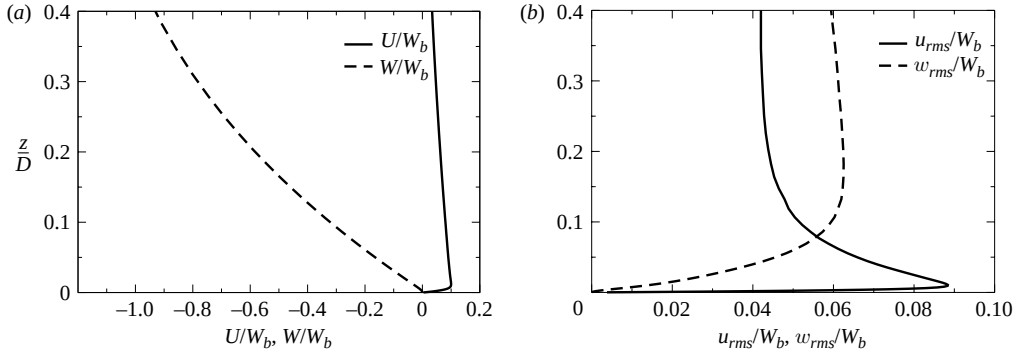

FIGURE 12. (*a*) Profiles of the mean axial and radial velocities, and (*b*) of the r.m.s. of the axial and radial velocity fluctuations along the centreline.

everywhere on the centreline (see figure 12*a*). As a result, the production of turbulent kinetic energy becomes negative in the wall vicinity.

Figure 11 shows the profile of the production of turbulent kinetic energy on the centreline of the jet compared with the experimental results of Geers *et al.* (2004). The present LES results agree very well with the experimental findings and provide additional data in the regions which were inaccessible to measurements. For example, experiments showed a switch of P_k from positive to negative values, but because of severe limitations, could not capture the maximum negative P_k, nor its subsequent decrease to zero on the wall, as obtained by LES.

The radial evolution of the turbulence energy production P_k is presented in figure 13(*a*) while the energy k itself in plotted in figure 13(*b*). Immediately after the stagnation point, the flow accelerates and a wall boundary layer is being formed. The wall shear gives rise to the positive turbulence energy production very close to the wall. However, the region of negative P_k (denoted by a chain line) persists up to $r/D \approx 1.5$, though gradually shifted somewhat away from the wall by the positive production due to near-wall shear. For example, at $r/D = 0.5$, P_k has a distinct,

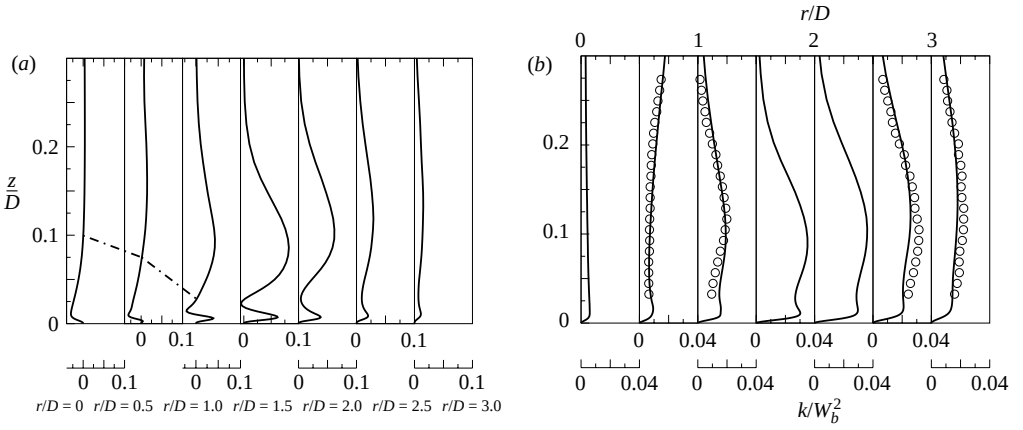

FIGURE 13. (*a*) Production of the turbulence kinetic energy and (*b*) the kinetic energy profiles at several locations in the wall-jet region.

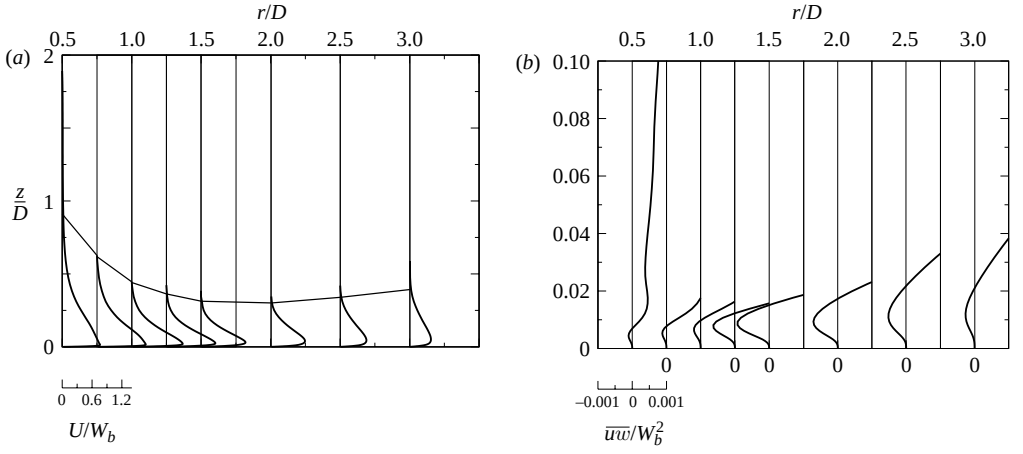

FIGURE 14. Development of the wall-jet: (*a*) radial velocity profiles (with indicated wall-jet edge); (*b*) turbulent shear stress $\overline{uw}$, at different distances from the jet centre.

but weak positive peak very close to the wall. Beyond this narrow region, P_k is negative again up to $z/D \approx 0.7$. The maximum production of turbulent kinetic energy in the wall layer occurs at $r/D \approx 1.5$, already in the well-established wall jet. The profiles of the turbulent kinetic energy (figure 13*b*) have been compared with the experimental data of Cooper *et al.* (1993). The overall agreement can be regarded as fully satisfactory, with minor discrepancies at $r/D = 1.0$, where the LES results show somewhat higher values of k, and further downstream at $r/D = 2.5$, where in the outer shear layer the LES peak in k is slightly lower than the measured one.

As the flow deflects radially, roughly at $r/D \approx 1$, a radial wall jet begins to form. Initially, the wall-jet is very thin and the fluid is subjected to a strong acceleration, as illustrated by a sequence of radial velocity profiles in figure 14(*a*). The flow accelerates up to $r/D \approx 1.3$, when the radial spreading and the subsequent growth of the wall-jet thickness causes the fluid to decelerate, enhancing further turbulence production in the near-wall region. Strong shear in the outer shear layer also gives

rise to turbulence energy production, generating double-peak shapes of both the P_k and k profiles (figure 13). The near-wall peak exceeds significantly that in a constant-pressure boundary layer, as also detected by several experimental studies of wall jets.

Another feature of the wall jet is the development of the turbulent shear stress $\overline{uw}$ and its correlation with the mean velocity. Figure 14(b) shows the evolution of $\overline{uw}$ along the impinged wall (only the near-wall values are presented) in parallel with the radial velocity. The maximum (negative) shear stress occurs between the positions $r/D = 1.0$ and $r/D = 1.5$. In addition to the well-known fact that the positions of the zero shear stress do not coincide with those of the maximum mean velocity – implying a negative shear contribution to the production P_k in the region in between, there are other features that show a lack of correlation between $\overline{uw}$ and the mean velocity gradient $\partial U/\partial z$. For example, at $r/D = 2.0$, the shear stress $\overline{uw}$ is higher than at $r/D = 1.25$, whereas figure 14(a) shows that the mean-velocity gradient at $r/D = 1.25$ is significantly larger than at $r/D = 2.0$. This means that the turbulent shear stress in the wall-jet is not proportional to the mean-velocity gradient as assumed in the eddy-viscosity hypothesis. A possible explanation for the decorrelation between the shear stress and mean velocity, manifested in the shift of the maximum shear towards the wall is most probably a strong turbulent diffusion by which eddies from the free jet shear layer penetrate deep into the boundary layer, increasing the level of the near-wall shear and wall friction.

The evolution of the kinetic energy and the shear stress is obviously governed by the sequential acceleration and deceleration of the fluid in the wall layer, but even more by the effects of the large-scale structures originating in the free-jet shear layer and interacting with the wall boundary layer. Further discussion is provided below in the analysis of the time dynamics of the vortical and turbulence structure.

4. Impinging jet structures

We consider now the instantaneous fields and identify coherent structures using different eduction methods aimed at elucidating the dynamics of vortical structures and turbulence in different regions of an impinging jet and their effect on and correlation with the wall heat transfer.

Figure 15 shows a three-dimensional impression of the instantaneous field of the complete impinging jet; for the sake of illustration, several coherent and incoherent large-scale vortical structures identified by the pressure contours in a single snapshot have been artificially superimposed on the instantaneous pressure field. An insight into the interior of the complete flow can be gained from figure 16, where a 90° segment has been removed to show the interior fields. Figure 16(a) shows the complete pressure field whereas figure 16(b) combines the pressure at the horizontal wall surface with the velocity field (intensity contours) on the vertical cut-planes. We can distinguish clearly the three characteristic zones, the free jet, the stagnation region and the radial wall jet, each with its own dynamics.

Free jet zone. In the initial zone (from $z/D = 2.0$ to $z/D \approx 1$, the flow features the typical dynamics of a free round jet, elaborated in details in the literature, e.g. Yule (1978). The issuing jet interacts with the ambient fluid triggering the growth of the shear layer, which, in the end, leads to the jet core being consumed. One of the characteristics of the jet configuration adopted here ($H = 2D$) is that the jet core does not disappear before the jet impacts the plate: the nozzle-to-wall distance is not sufficiently large to produce a fully mixed jet. Natural instabilities of the

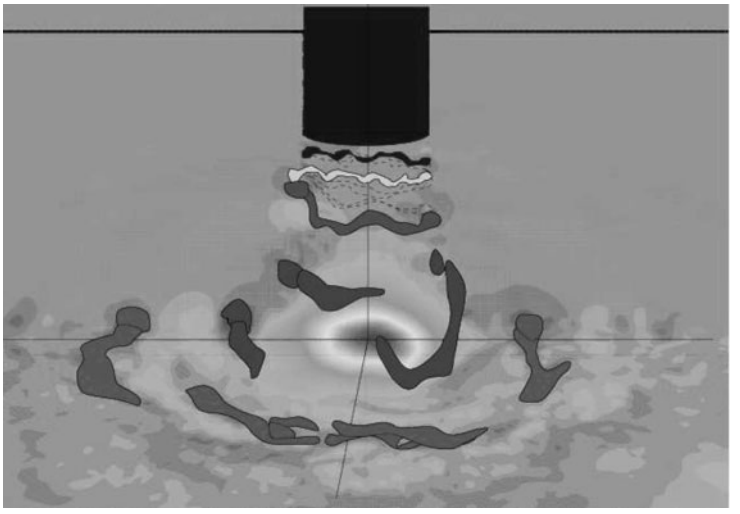

FIGURE 15. Artistic impression of the jet ring vortices and their evolution and breakdown.

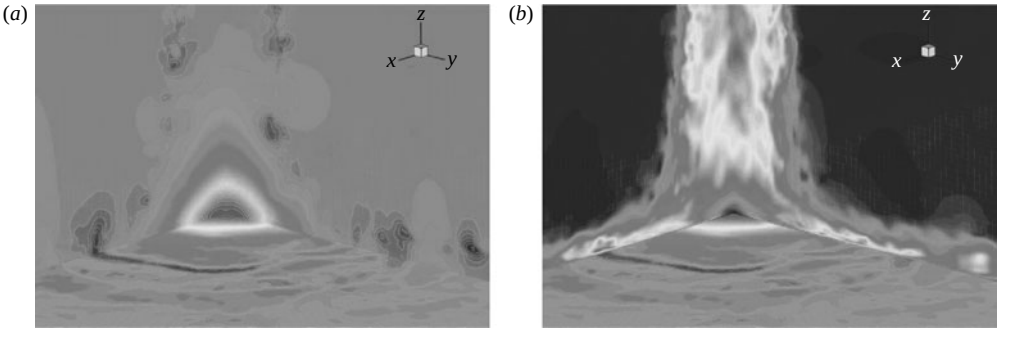

FIGURE 16. Instantaneous snapshots. (*a*) Pressure field; (*b*) velocity intensity (vertical planes) and pressure field (horizontal plane).

Kelvin–Helmholtz type develop in the initial shear layer, leading to the creation of a street of roll-up vortex rings, as illustrated by a snapshot of the instantaneous vorticity magnitude (figure 17*a*), obtained with Grid IV that accounts for the real pipe wall thickness. These vortex rings are convected downstream, pairing and coalescing with neighbouring rings, with increased azimuthal wave instability which gradually reduces their circumferential coherence. The distance between them increases with the distance from the nozzle exit. The low-pressure regions in the instantaneous pressure field (figure 17*b*) clearly indicate the eddy centres in the initial shear layer. Further downstream, the low-pressure regions grow, associated with an increase of the scales of ring vortices. With an increase of the distance from the nozzle, the ring vortices lose their phase lock and the coherent ring-like form.

The ambient fluid is entrained into the shear layer and the velocity and stress fields gradually lose their similarities with the velocity and stress fields in the pipe flow. The continuous stretching and deformation of vortex rings owing to azimuthal instabilities are shown by the vorticity magnitude in figure 18. Although the plot of azimuthal vorticity would be more appropriate to define the vortex ring, this component dominates the total vorticity and its plot would show a very similar

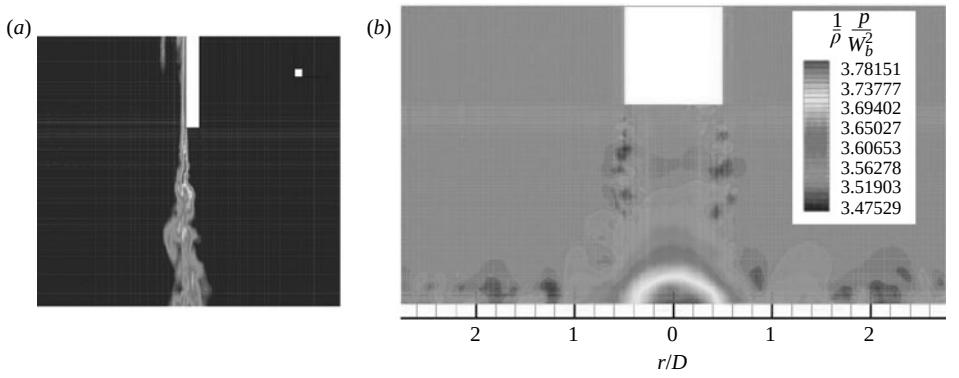

FIGURE 17. (*a*) Instantaneous vorticity-magnitude, Grid IV; (*b*) instantaneous pressure field, Grid II.

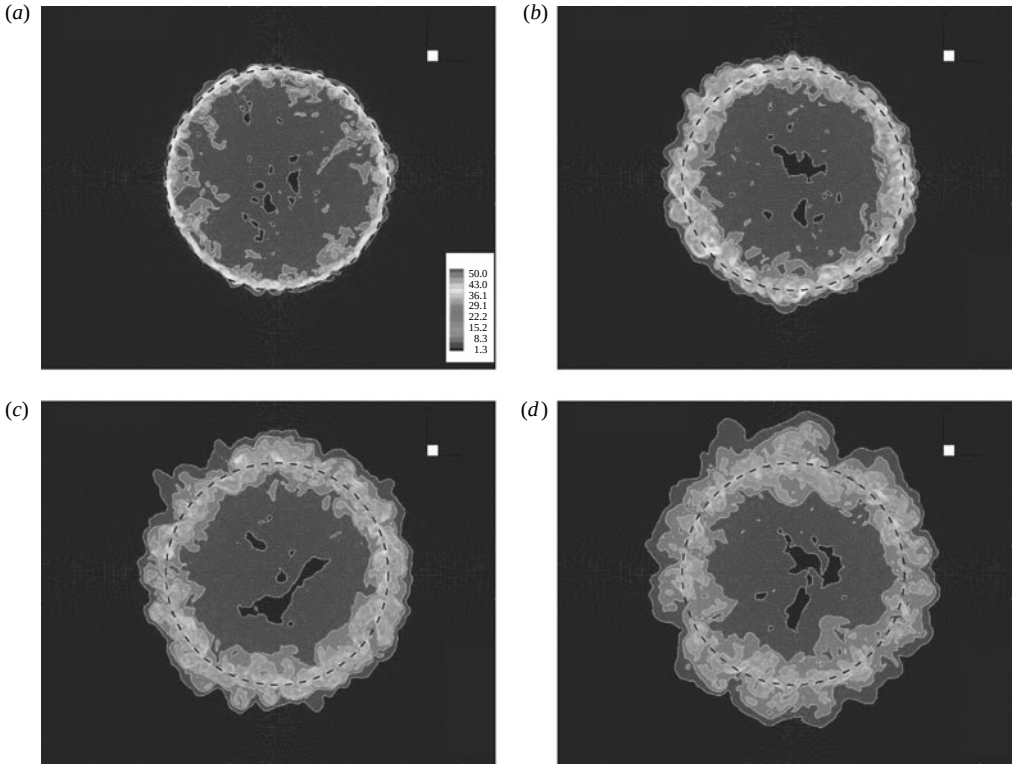

FIGURE 18. Stretching and deformation of a circular shear layer visualized by the the instantaneous vorticity-magnitude (grey scale) in four horizontal planes in the free jet zone. (*a*) $z/D = 1.95$, (*b*) 1.72, (*c*) 1.50, (*d*) 1.25.

picture.). Close to the nozzle exit, e.g. at $z/D = 1.95$, the vortex ring is very thin with high vorticity concentrated in a relatively regular ring around $r/D = 0.5$, with a large number of small azimuthal instabilities (figure 18*a*). However, in contrast to distinct and persistent smooth ring shapes seen in a forced round jet (and also at a much lower *Re* number of 6000 and with a large $H/D = 10$) by Tsubokura *et al.* (2003), further from the nozzle exit, at $z/D = 1.5$ and especially at $z/D = 1.25$,

the ring vortices become highly deformed with distinct vortical nests distributed over the vortex ring circumference (figure 18*c*, *d*). These three-dimensional patches of concentrated vorticity serve as precursors of large-scale turbulent eddies, which subsequently impinge on the wall. At $z/D = 1.75$, we can count over 30 distinct vortical nests over the circumference (from which the natural frequency of the azimuthal instability could be inferred by a conditional data processing, but this issue, being pertinent only to the initial free jet, is outside the focus of our work). These structures grow and pair so that their number at $z/D = 1.25$ is already reduced to about half. At this stage, these vortical nests, while still circumferentially interconnected, begin to acquire features of typical large-scale turbulent eddies, i.e three-dimensional fluid regions with a high concentrated vorticity, but without a distinct vorticity orientation. Although the ring-coherence has disappeared, these large-scale eddies can still be regarded as coherent turbulent structures, distinct from the embedded and surrounding stochastic small-scale turbulence. Prior to their impingement, the natural growth of these eddies owing to stretching is accompanied also by vorticity diffusion both inwards into the jet core and outwards.

At a certain distance from the nozzle exit, the ring vortical structures break down. However, prior to that, the deformed ring vortices become tilted with respect to the impinged plane. Owing to the tilting and irregularity of the vortex breakdown, the axial symmetry is lost and the coherent large-scale eddies, which were originally parts of the ring-vortex structure, strike the target wall at different time instants. Together with the natural pressure pulsation due to the jet periodic shrinking and expanding caused by the formation of a ring vortex street, the asymmetric impingement of large-scale eddy structures causes a jet flapping and occasional precessing around the jet axis. Such a periodic and asymmetric impingement of strong large-eddy structures is believed to be instrumental in the surface renewal process that enhances the stagnation heat transfer. An attempt to visualize this process is shown in figure 19, where the coherent eddy structures are identified by the constant-pressure contours. Different colours/shades indicate the eddy structures at different distances from the target wall. The pressure iso-surfaces reveal initially the ring-like structures in the jet shear layer, which grow and break down into large-scale coherent eddy structures in which the remnants of ring vortices can still be discerned.

A sequel of snapshots of the instantaneous velocity field very close to the wall ($z/D = 0.005$) is depicted over a typical period (see below) in figure 20 showing the intensity of the fluid velocity. White patches denoting high local velocity reflect the strong acceleration of the fluid being pushed away radially after the impingement of the large-scale structures. Although circular patterns can be discerned at larger distances from the jet centre, the near-wall structure is never circumferentially fully closed and the zones of equal or similar velocity do not form continuous rings. Locally, the peak velocity can be twice as high as in nearby regions. The peak velocities at different instants are located at different azimuthal locations, confirming the above conjecture of asymmetric impact of the large eddies on the wall at different time instants.

The natural frequency of the shear-layer instabilities is parameterized by the Strouhal number $St = fD/W_b$, where f is the frequency of the roll-up eddies. In an impinging jet, next to Re number and initial velocity profile and turbulence state, St also depends on the nozzle-to-plate distance and other factors. Yule (1978) found $St \approx 0.6$ for $Re = 21\,000$ and at the station $z = 0.4D$ in a free round jet issuing from a smoothly shaped nozzle. He observed the decrease of St further downstream along the jet owing to vortices growth and coalescing, approaching a constant value

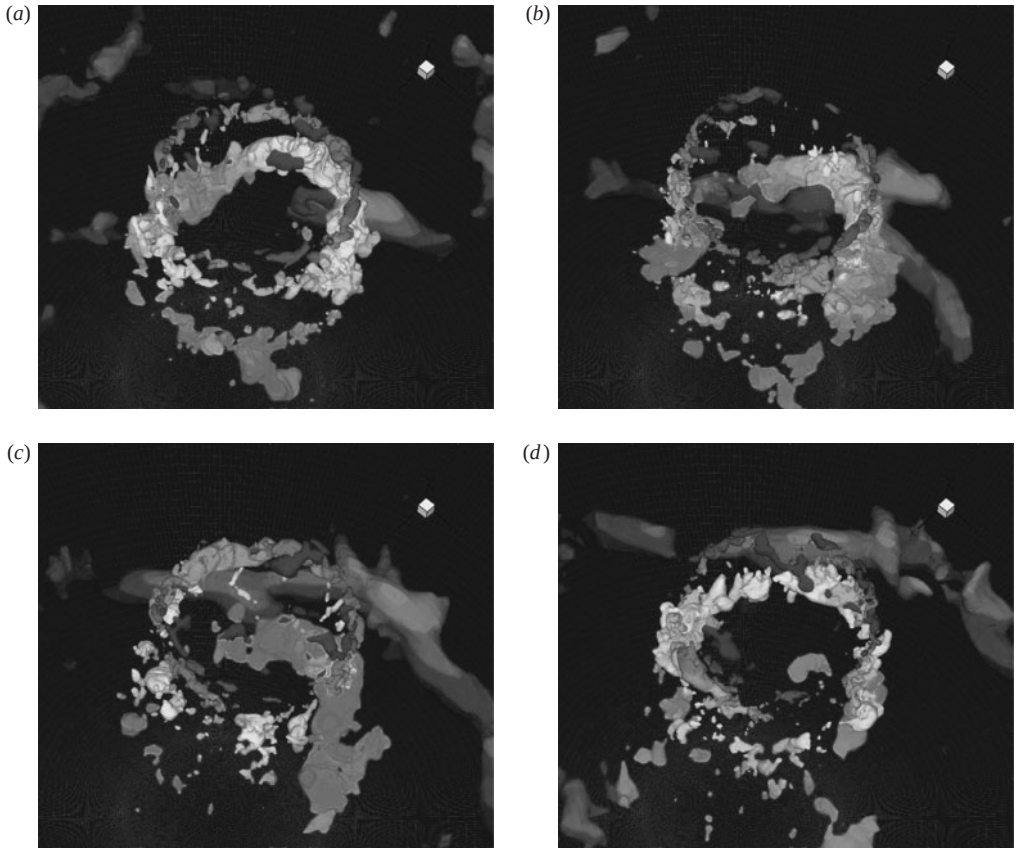

FIGURE 19. Breakdown of vortex rings and formation of large-scale eddies, approaching the target wall: iso-surfaces of pressure coloured by the distance from the impingement wall. (*a*) $t/\tau = 0$, (*b*) 1/3, (*c*) 2/3, (*d*) 1.

of 0.33–0.4 at about 5–6 nozzle diameters. Han & Goldstein (2003) found $St = 0.65$ for $Re = 8000$ and $St = 0.6$ for $Re = 120\,000$ at $z/D = 1$. For a smaller Reynolds number, Tsubokura *et al.* (2003) found that a round jet ($Re = 6000$ and $H = 10D$) has a distinct unstable mode of $St = 0.37$, which remains more or less the same at different distances from the jet exit ($H/D = 3$–8). In order to detect the characteristic frequency of the shear-layer instabilities, we plotted the energy-density spectra, obtained from a time series of the velocity magnitude. In the initial shear layer close to the jet exit from the pipe (at $z/D = 1.9$ and $r/D = 0.5$), the spectrum indicated a relatively mild peak at $St \approx 0.64$, which is close to that measured at the exit of a free air jet at a similar Re number by Yule (1978), though different from the results reported by Tsubokura *et al.* (2003). The origin of this difference could be attributed to the differences in the Re number and H/D ratio. Similar roll-up vortices are detected further downstream at the edge of the wall-jet, as can be seen in figure 17, (see also figure 23), showing again a circular ring-like distribution of vorticity, but far from having a regular toroidal shape. Their locations vary and a distinct St number of these structures at the wall-jet edge could not be clearly identified.

The characteristic frequency of the large ring-like vortical structures can be confirmed in figure 19, which shows that the structure shapes in figures 19(*a*)

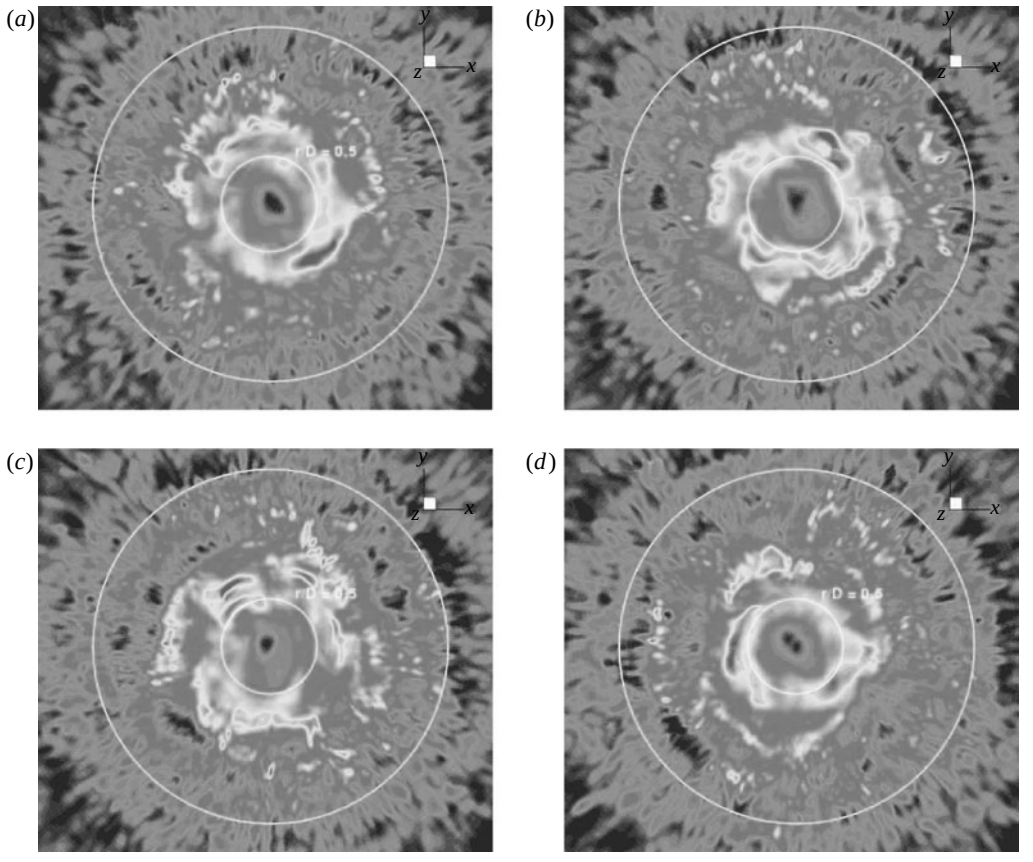

FIGURE 20. Instantaneous velocity-magnitude fields close to the wall surface at different time instances over the characteristic period $z/D = 0.005$. (*a*) $t/\tau = 0$, (*b*) 1/3, (*c*) 2/3, (*d*) 1.

and 19(*d*) are similar and correspond to the beginning and the end of a period, which indicates the time period of about $\tau = 3$ s, corresponding to $St \approx 0.64$. (Note that LES was performed for a fictitious fluid and configuration with $D = 2.0$ m and $W_b = 1.0\,\mathrm{m\,s^{-1}}$ and a viscosity matching the Reynolds number $Re = 20\,000$; for the experimental situation of Geers *et al.* (2006) with $D = 36$ mm and $W_b \approx 9\,\mathrm{m\,s^{-1}}$, using air, this corresponds to a frequency of about 160 Hz.). A similar conclusion emerges from figure 20 where again the structural patterns for $t/\tau = 0$ and $t/\tau = 1$ seem close to each other and different from the other two snapshots in between.

Stagnation region. The flow structures in the stagnation region were difficult to identify. No distinct organized eddy structures were observed. High static pressure and the wall-blocking effect cause transfer of energy from the turbulence field back to the mean flow. The instantaneous velocity field shows the absence of the small-scale motion in the centre of the stagnation region (figure 20). This region is influenced by the dynamics of large-scale eddies which come from the jet mixing layer. Figure 20 (for more details see figure 25) reveals that the iso-contours of the instantaneous velocity in the wall-parallel plane at $z/D = 0.005$ from the impingement wall, are stretched in the direction perpendicular to the circular regions of high velocity. The flow acceleration in the wall-jet region, enhanced by the impact of large eddies

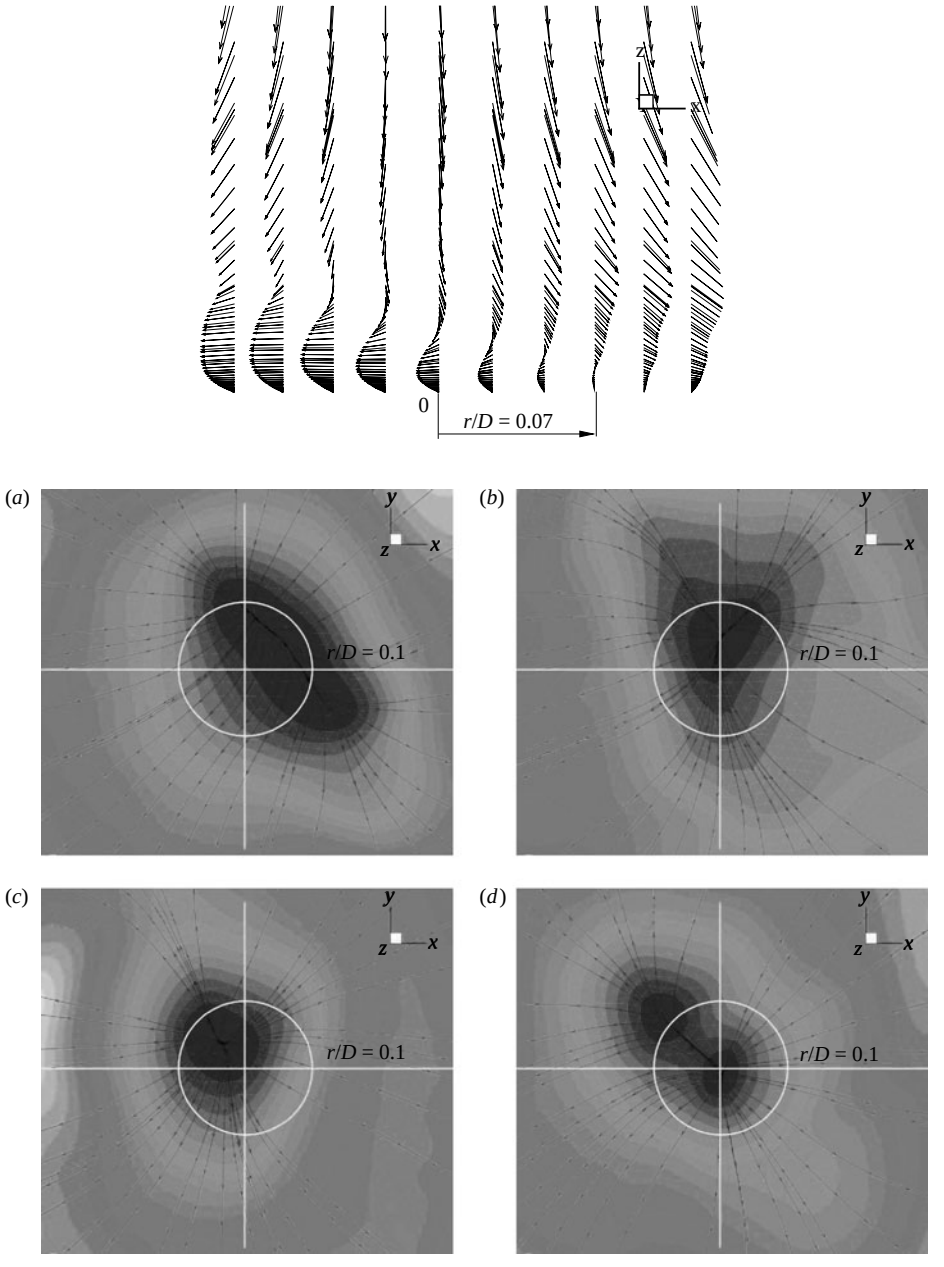

FIGURE 21. Top: instantaneous velocity-vector field in the (x, y)-plane around the jet centre. $(a–d)$ Stagnation point at different times (instantaneous streamlines and contours of the instantaneous velocity). (a) $t/\tau = 0$, (b) 1/3, (c) 2/3, (d) 1. $z/D = 0.005$.

advected from above, causes these deformations. The instantaneous velocity vectors in the (x, y)-plane indicate a dislocation of the impingement position from the centre of the jet (figure 21, top). The snapshots of the instantaneous velocity and corresponding streamlines, in the horizontal plane at $z/D = 0.005$ above the impingement wall, reveal the movement of the impingement point (figure 21). Note that the impingement 'point' temporarily becomes a line (figure 21a) and even splits into two separate impingement

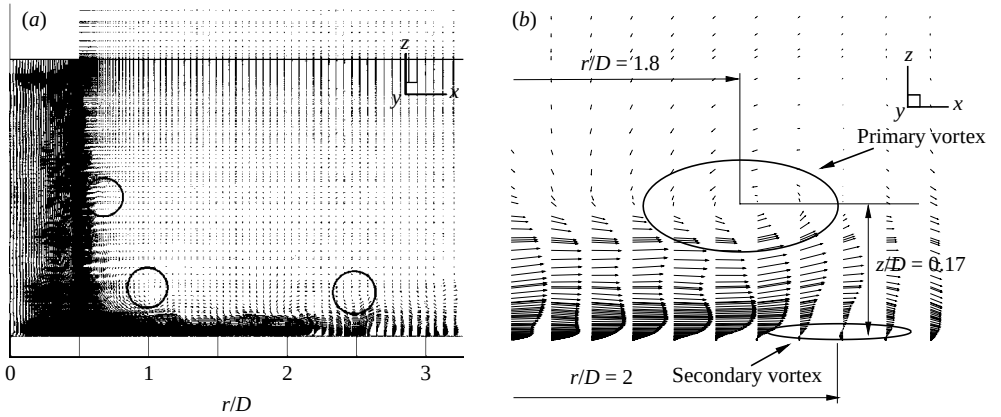

FIGURE 22. Instantaneous velocity-vector field: (*a*) a full view with three vortical cores (encircled); (*b*) an enlargement in the wall-jet region around $r/D = 2$.

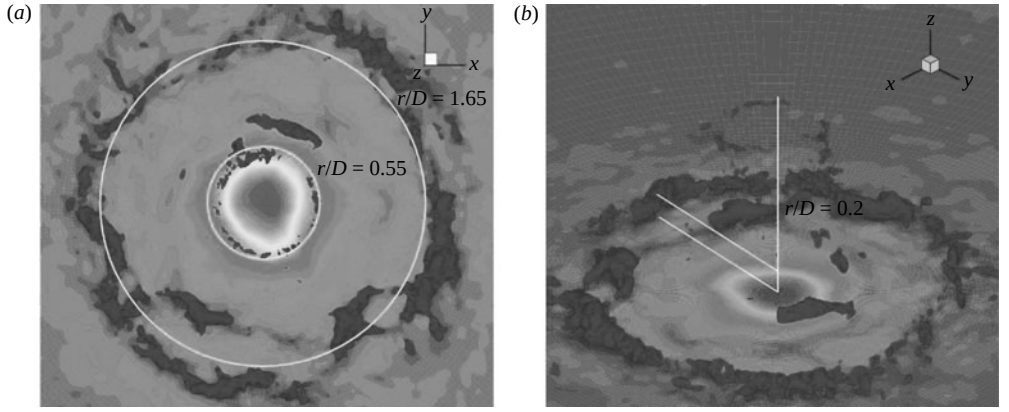

FIGURE 23. Iso-surface of the instantaneous pressure. (*a*) top view; (*b*) side view.

regions (figure 21*d*). The maximal impingement-point dislocation is found to be $r/D = 0.1$. This impingement-point oscillation suggests a jet flapping or precessing, as detected also experimentally by Geers *et al.* (2006), which is believed to be caused by the instability and asymmetric breakdown of the originally ring-like large-vortex structures originating from the jet-shear layer. The oscillation of the impingement position can additionally enhance the fluctuations in the radial direction.

Wall jet. The development and organization of the flow structures as the jet deflects from the impingement plate are also intriguing. Immediately after the deflection, a thin boundary layer is formed in which fluid undergoes a strong acceleration, to be superseded by a strong deceleration. An overall view of the development of the wall jet is given in figure 22(*a*), which shows a snapshot of the instantaneous velocity vectors. After scrambling of the ring-like structures in the impingement zone, figure 22(*a*) and especially figure 23 show a new tendency towards vortical self-organization in the form of new roll-up ring-like vortical structures formed at the wall-jet edge shear layer: three cores of such vortical rings can be discerned, with especially well-organized structure with a visible azimuthal coherence and unbroken circumferential connections at $r/D \approx$ 1.6–2.0

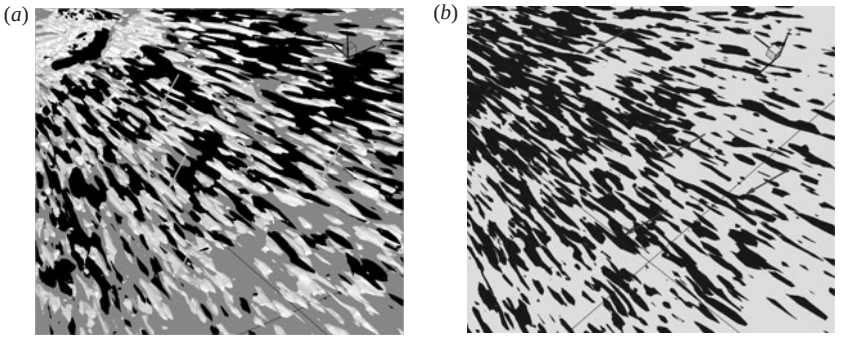

FIGURE 24. Near-wall streaks identified by iso-surfaces of Q parameter. (a) A little further from the stagnation, black $Q = -0.1$; white: $Q = 1.0$; (b) wall-jet region, black $Q = -0.1$.

The formation of the roll-up vortices at the wall jet edge is the consequence of the Kelvin–Helmoltz instabilities, as in the shear layer of the free jet. However, the pattern seen in figures 22 and 23 is not characteristic of a slot wall jet and it seems likely that the well-organized ring structure is triggered by the remnants of the free-jet ring vortices, which survive the impingement and deflect radially by an accelerating fluid. Strong azimuthal rotation of the toroidal vortices affects the flow in the near-wall region. The most interesting consequence is the local flow separation seen in figure 22(b), with a counter-rotating wall-attached bubble with internal recirculation, denoted as 'secondary vortex'. It can be seen that the wall recirculation bubble is rolled up between the plate surface and the large-scale toroidal vortex at the wall-jet-edge shear layer (denoted as 'primary vortex'). Both vortical structures are strongly stretched in the radial direction before they are destroyed and entrained into the turbulent wall-jet. The existence of these ordered structures was confirmed by a smoke-wire visualization technique (Popiel & Trass 1991). As discussed below, the local separation has a strong effect on the local heat transfer and is closely linked with the non-uniformity in the Nusselt-number distribution.

It is known that the near-wall regions in channel and pipe flows are characterized by the elongated streaky structures. However, the round wall-jet is subjected to a strong deceleration due to radial flow spreading, while the flow structures are subjected to stretching in the azimuthal direction for the same reason. Therefore, it can be expected that the roll-up of eddies with their rotation axis aligned with the azimuthal direction will be enhanced, and this dynamics should reflect in the organization of the near-wall streaks. A question may be raised on what would happen with near-wall streaks when subjected to radial spreading and consequent adverse pressure gradient. For an insight, we attempted to identify the streaky structure, using – as the coherent vortex identifiers, the Q-criterion defined as $Q = -0.5(S_{ij}S_{ij} - \Omega_{ij}\Omega_{ij})$, where $S_{ij} = 0.5(\partial U_i/\partial x_j + \partial U_j/\partial x_i)$ is the strain rate and $\Omega_{ij} = (\partial U_i/\partial x_j - \partial U_j/\partial x_i)$ is the rotation rate tensor. Q can be interpreted as a measure of the magnitude of rotation relative to the strain rate. A positive value of Q means that rotation prevails over strain and vice versa. Two different ranges for Q were used.

Figure 24 shows the iso-surface of $Q = -0.1$ and $Q = 1.0$ in the region very close to the impinged wall at several locations, computed from the instantaneous velocity field. The stagnation region, figure 24(a) seems rather void of streaks, and those few observed all have negative Q values ($Q = -1.0$) indicating a very high strain rate. The black streaks prevail very close to the wall in all other regions. However, further

in the radial direction a large number of white streaks ($Q > 0$) appear, indicating a prevailing rotation, first in the form of broken ring patterns, and then with radial orientation, but all at a distance further from the wall than the black streaks. This is clearly seen in figure 24(*b*), although for the adopted Q values the streak population gradually becomes less dense when moving in the radial direction further away from the stagnation point. The streaks are subjected to stretching in the azimuthal direction owing to the radial-flow spreading. As a consequence, a single streak occasionally splits into two parts and forms two separate streaks. However, the opposite pattern is observed too. At several locations, two separate streaks merge and form a single larger streak. While streak splitting is caused by the radial-flow spreadings, the mechanism behind the streak merging (most probably associated with vortex pairing and coalescing) is not fully clear. It is possible that this is also linked to a strong adverse pressure gradient, since this phenomenon is observed mostly in the part of the wall-jet subjected to a strong deceleration. The locations where the streak splitting or merging are observed, are pointed out by arrows in figure 24.

5. Thermal signature of the flow structure and heat transfer

We consider the thermal imprints of the vortical and turbulence structures on the impinged wall and their correlation with heat transfer. First, the velocity field very close to the wall (at $z/D = 0.005$) represented by the instantaneous streamlines and velocity intensity contours, is shown in parallel with the instantaneous wall temperature and Nusselt-number fields, taken at the same time instants (figure 25).

Figure 25(*a*) shows a relatively regular streamline pattern illustrating the radial flow spreading. Up to $r/D \approx 1.0$, the streamlines have fairly regular radial directions, and then tend to agglomerate into identifiable groups where they remain almost parallel, with inevitable spacing in between to satisfy the continuity. This suggests a formation of individual radial streams, which can be associated with different streaks identifiable in figure 24(*a*). Further away, at $r/D \approx 1.5$, which, as discussed below, corresponds roughly to the Nusselt-number dip, these structures break and the streamlines begin to wiggle and meander, most probably because of strong adverse pressure gradient, and this agglomeration is visible all the way up to $r/D \approx 2.5$. The velocity iso-contours in figure 25(*b*), although, of course, closely related to the streamline pattern, provide more details about the local structures and their thermal imprint on the wall (figure 25*c*, *d*).

The distribution of the instantaneous surface temperature (figure 25*c*), together with the corresponding instantaneous Nusselt number (figure 25*d*), shows that the lowest temperature is found in the stagnation region owing to the efficient cooling effect of jet impingement. The instantaneous velocity field (figure 25*b*), corresponds to the instantaneous Nusselt-number in figure 25(*d*). As noted earlier, the large-scale eddies, which impact the wall, deform the iso-lines of the velocity-magnitude in the stagnation region. The oval iso-lines indicate stretching of the flow structures in the direction dictated by these large-scale structures. The region of high heat-transfer coefficient is not circular, but also stretched in the direction that nearly corresponds to the stretching direction of the velocity iso-lines.

However, as seen in figure 26(*a*), which shows a snapshot of the instantaneous Nusselt number and skin-friction coefficient over the wall, a full instantaneous correlation between the two fields is lacking. The classic Reynolds analogy is not fulfilled, especially around the stagnation point where the velocity (and wall shear) go to zero, whereas heat transfer reaches its maximum. Nevertheless, the similarity

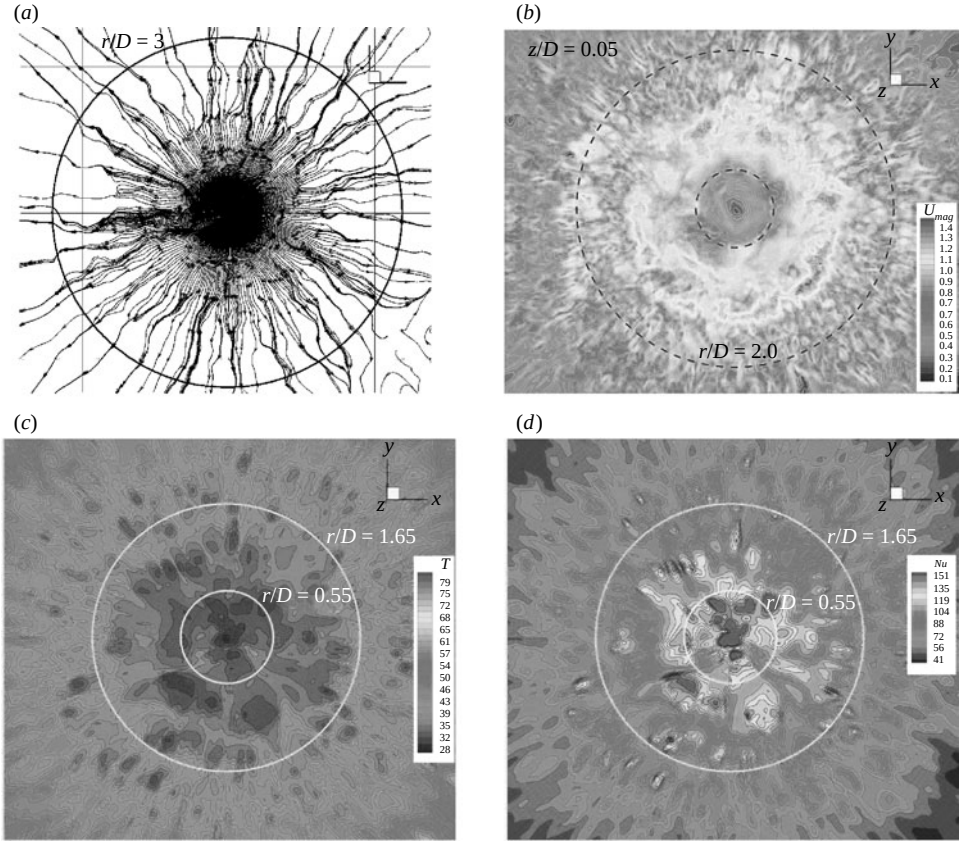

FIGURE 25. Instantaneous velocity and thermal fields in the wall-parallel plane at $z/D = 0.005$: (*a*) streamlines; (*b*) velocity magnitude; (*c*) surface temperature; (*d*) Nusselt number.

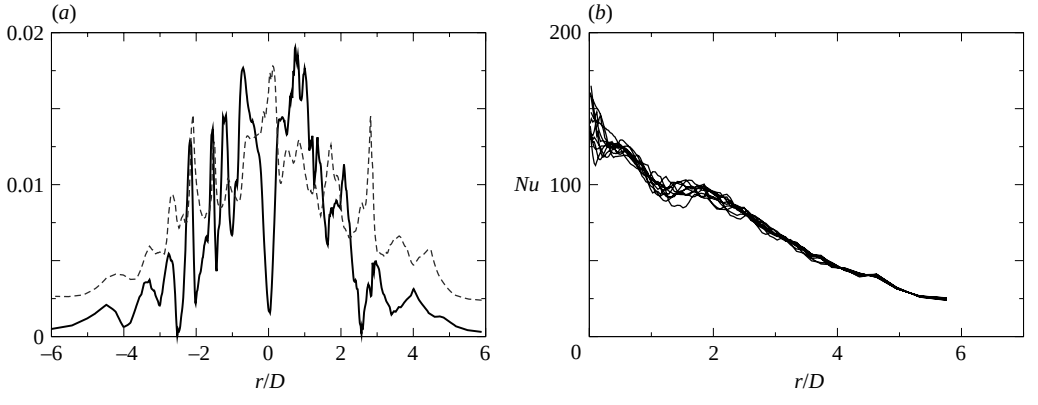

FIGURE 26. (*a*) - - -, Instantaneous Nusselt number Nu and skin friction ——, C_f; (*b*) a series of snapshots of the radial Nu distributions.

between the two signals a little further from the stagnation point is striking. The signals are not symmetric, showing a very close phase correlation in the left-hand branch, but being significantly out of phase on the right-hand side. Both signals show

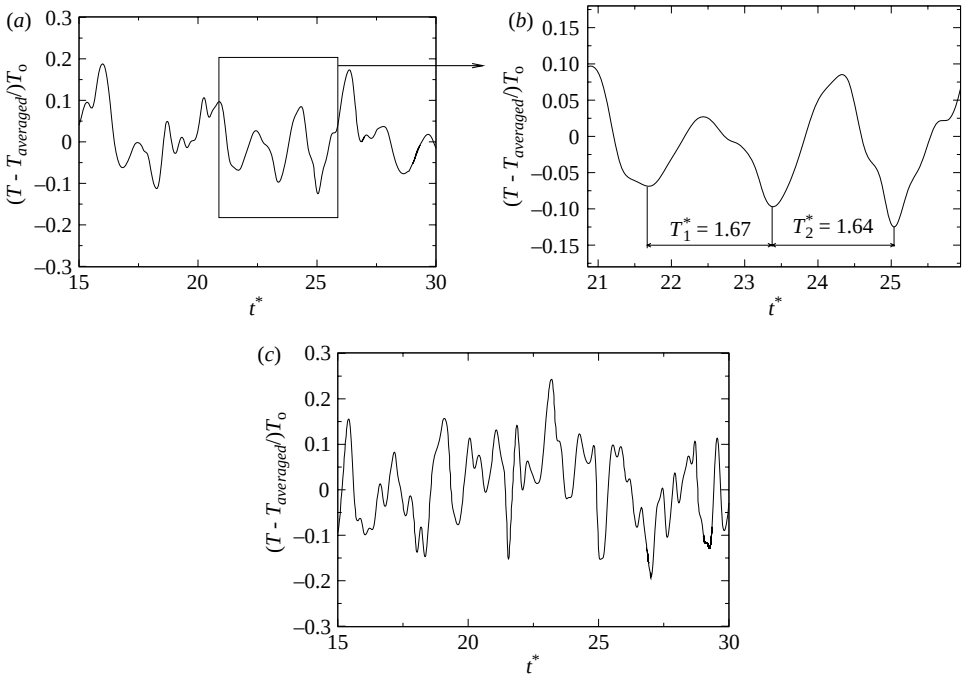

FIGURE 27. (*a*, *b*) Histograms of the wall temperature in the stagnation point, and (*c*) at $r/D = 1.0$; $t^* = tW_b/D$.

high peaks associated with large-scale eddy structures, which confirm the conjecture that the impingement of large-scale eddies plays a key role in heat transfer.

Figure 26(*b*) shows a series of instantaneous realizations of the Nusselt-number distribution over the impinged wall. Despite the scatter indicating vigorous time dynamics, especially in the impingement region ($r/D \approx 2$), the distribution reveals the characteristic shape for the $H/D = 2$, with two peaks, one at the stagnation point and the second one at about $r/D \approx 2.0$, with a dip at $r/D \approx 1.5$. We consider now in more detail each of the characteristic *Nu* regions.

The time histories of the wall temperatures at two positions, $r/D = 0$ and $r/D = 1.0$, are shown in figure 27. Both signals have unsteady and oscillating behaviour. However, more regular oscillations with somewhat smaller amplitude occur in the wall temperature signal at the stagnation region than in the signal at $r/D = 1$. Although the temperature signal at $r/D = 0$ does not show a regular sinusoidal periodicity, it clearly indicates jet flapping. The time interval between the two local maxima indicates the flapping period $\tau^* \approx 1.65$, which appears to be roughly the same as the period detected in the free jet. This means that large-scale eddies originating from the breakdown of the ring vortices impinge on the wall with the frequency of their parent toroidal structure, suggesting an alternating impingement of eddies coming from the opposite sides of the jet. Of course, this pattern moves also in the azimuthal direction, leading to a periodic impression of eddy-structure processing around the geometrical jet centre.

The above finding confirms the assumption that the temperature fluctuations in the stagnation region are determined by the impingement of the large-scale vortical structures which originate from the jet shear layer. This is also confirmed in figure 26 where the largest oscillations in the *Nu* number profile are found in the stagnation

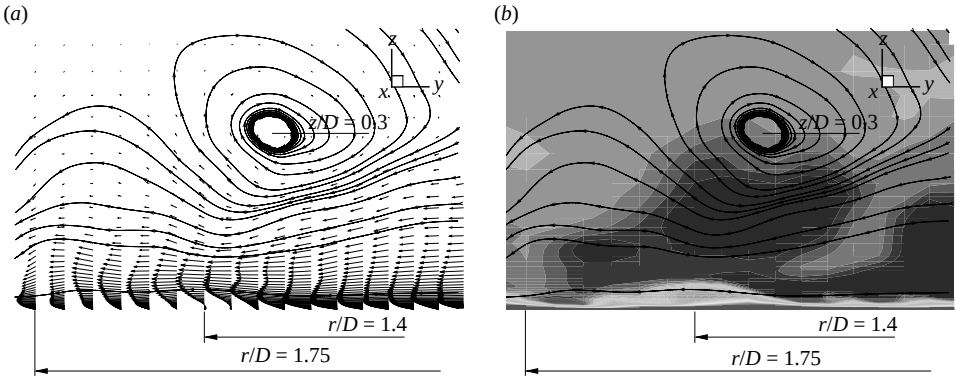

FIGURE 28. Simultaneous snapshots of the (*a*) velocity and (*b*) temperature fields in an azimuthal plane in the wall-jet region around separation bubble, with the superimposed streamlines.

region. The impact of these structures on the wall causes a thinning of the boundary layer and a high fluid acceleration around the stagnation point leading to the minimum in the instantaneous temperature signal. As the eddy structures deflect radially, the thermal boundary layer becomes thicker and the wall temperature starts to increase. The local maximum is reached when the incoming eddy does not yet fully affect the wall and the outgoing eddy is still far away. Irregularities in the wall temperature signal at the stagnation point are due to the nonlinear effects associated with turbulence. Chung & Luo (2002) have found that for smaller Reynolds number, the temperature signal in the stagnation region is almost sinusoidal.

A feature of the jet configuration here investigated ($H/D = 2$) is the occurrence of a second maximum in the Nusselt-number distribution. For higher nozzle-to-plate distances, the second maximum becomes less pronounced, whereas it totally disappears for distances larger than $4D$. The second maximum is also affected by the Reynolds number in the sense that it increases with the increase in the Reynolds number. It is indicative that the second maximum diminished for jets with jet core shorter than the nozzle-to-wall distance. This means that the existence of the jet core has a profound effect on the heat-transfer coefficient. The origin of the second maximum is, however, still disputable.

As the radial distance from the stagnation point increases, the Nusselt number starts to decrease and reaches its minimum at $r/D = 1.5$. The position of the Nusselt-number minimum coincidences with the location where distinct wall-attached separation bubbles were found. As mentioned earlier, the wall-attached vortices are created by the interaction of the large-scale vortices with the wall-jet. As a result, unsteady separation occurs, which is visible in the instantaneous vector field shown in figure 28(*a*). The thermal boundary layer is affected by the separation causing its thickening (figure 28*b*). The radial fluid motion causes a strong stretching of the wall-attached vortices leading to their breakup, detachment and entrainment into the wall-jet. Between the positions $r/D = 1.3$ and $r/D = 1.8$, the radially stretched islands of low Nusselt number occur (figure 25*d*). These are probably the regions where instantaneous separation occurs, resulting in a decrease of the heat-transfer coefficient. The breakup of the wall bubbles leads to subsequent enhancement of the local momentum and heat transfer and possibly to the occurrence of the second peak in the local Nusselt number. This leads to the conclusion that the interaction of the large-scale structures, originating

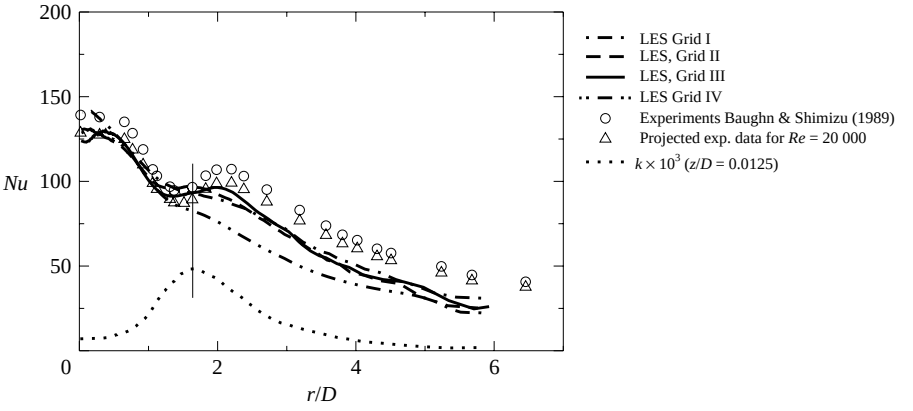

FIGURE 29. Time-averaged Nusselt number obtained with different grids.

from the jet shear layer, with the developed turbulent radial wall-jet plays a major role in the non-monotonic radial distribution of the convective heat-transfer coefficient.

5.1. *Time-averaged fields*

In view of the undisputed role of large-scale coherent eddy structure in heat transfer, a question arises of whether and how the Reynolds-averaged Navier–Stokes (RANS) approaches, used widely for computation of turbulent flows and heat transfer, can reproduce the time-averaged velocity and thermal field in flows dominated by unsteady large-scale eddy dynamics. In order to examine some of the basic RANS presumptions, we compare the time-averaged thermal imprint of the flow field and turbulence on the impingement plate, represented by the mean Nusselt number, wall-parallel profiles of the mean velocity, mean temperature and turbulence second moments (stresses and fluxes) at two wall-parallel planes very close to the impingement wall, $z/D = 0.0125$ and 0.05.

Compared with the measurements of Baughn & Shimizu (1989), the present LES returned the time-averaged heat-transfer coefficient, expressed in terms of the Nusselt number, with mixed success (figure 29). While agreement with experiments is very good in a broad region around the stagnation (for $r/D < 2.0$), a discrepancy appears at larger radii in the wall-jet region, where the LES Nusselt number shows the same monotonic decrease in the radial direction as in the experiments, but with systematically lower values with all the grids used. Both the dip and the second maximum are recovered by Grids I–III, but in LES they are milder and less pronounced than in the Baughn & Shimizu experiments. Apart from Grid IV, the other three grids produce similar results, though the best agreement with experiment is achieved with Grid III (a quarter of the full three-dimensional domain) which contained the largest number of grid cells. Assuming that the experiments are reliable, this indicates that the mesh resolution in the wall-jet region is still not sufficient in the region beyond $r/D = 2.0$. Recall that the resolution of Grid II in the radial direction in the region around $r/D \approx 2.0$ is $\Delta r^+ \approx 80$, which is just about the recommended limit for the streamwise spacing for attached boundary layers. This appears, however, still to be too coarse for accurately capturing the complex dynamics of the wall-attached separation vortex and its breakdown, together with the near-wall streaky structure, which both play significant roles in the heat transfer mechanism. We recall again, that our focus was on the stagnation region and no further grid refinement in the wall-jet regions was pursued because of the limitation on computer resources,

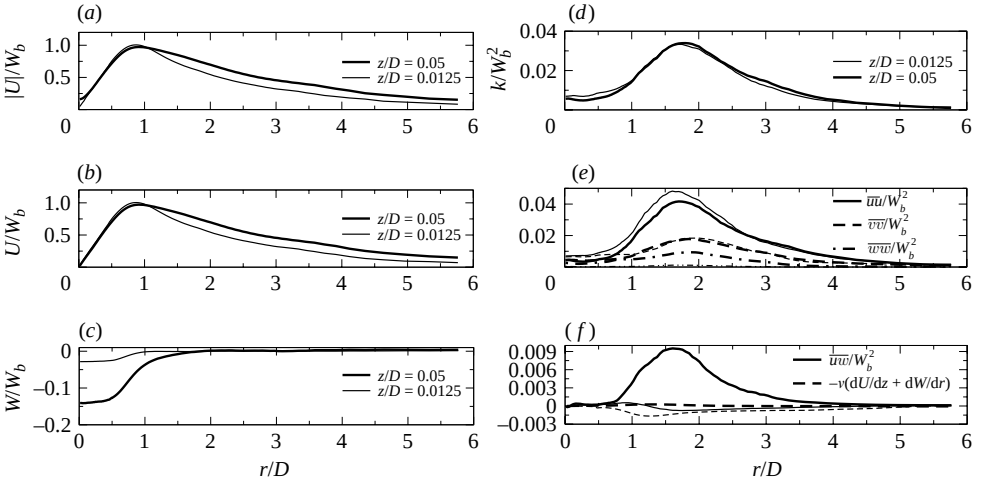

FIGURE 30. (*a–c*) Mean-velocity and (*d–f*) the turbulent stress components in the wall-parallel plane at $z/D = 0.05$ (thick lines) and $z/D = 0.0125$ (thin line).

but also because the effect of grid refinement seems to be clearly identified. Note that the simulation on Grid III shows a small Nusselt-number dip at the centreline, with the first maximum slightly displaced. As mentioned in § 1, such a displacement of the Nusselt-number peak in a similar configuration – though much more pronounced – has been reported by Ashforth-Frost & Jambunathan (1996*b*) and Lee & Lee (2000), whereas most other experiments show a clear maximum at the stagnation point.

The profiles of the mean velocity and stress components (figure 30) show similar behaviours for the two considered distances from the wall. The radial velocity U (figure 30*b*) shows a very strong gradient in the stagnation region owing to the deflection of the jet, reaching the maximum value at $r/D = 0.9$ and then begins to decrease. The 'axial' (wall-normal) velocity W is almost constant up to $r/D = 0.5$ (though with a much smaller value at $z/D = 0.0125$), but then decreases rapidly towards zero. Beyond $r/D = 2$, practically only the radial component exists. As noted earlier, the turbulent kinetic energy has relatively low values in the stagnation region. As the flow accelerates, k begins to increase. The maximum value occurs at $r/D = 1.8$. A major contributor to the turbulent kinetic energy is the $\overline{uu}$ stress component, whereas the wall-normal $\overline{ww}$ is smallest, as in all wall flows, and at $z/D = 0.0125$ becomes negligible indicating an approach towards the two-component limit. At $z/D = 0.05$, the shear stress $\overline{uw}$ follows the profile of k with the magnitude of roughly $0.3k$, just as in an ordinary boundary layer. It is uniform until $r/D = 0.5$, and then increases sharply towards a maximum value at $r/D = 1.7$, but remains positive everywhere.

Note that, according to the Boussinesq hypothesis, the minimum shear stress should appear around $r/D \approx 1.0$, where the radial velocity reaches its peak. However, it is clear that this is not the case and $\overline{uw}$ is not proportional to $(\partial\overline{U}/\partial z + \partial\overline{W}/\partial r)$ as the eddy-viscosity hypothesis presumes. At $z/D = 0.0125$, the shear stress $\overline{uw}$ shows a very different behaviour, changing the sign at $r/D \approx 1.25$. For comparison, the viscous shear stress is also presented (broken lines), showing its dominance at $z/D = 0.0125$, but negligible values at $z/D = 0.05$.

The profiles of k and $\overline{uw}$ in two planes in figures 30(*d*) and 30(*f*) do not show any correlation with the Nusselt number in the stagnation region, thus supporting the

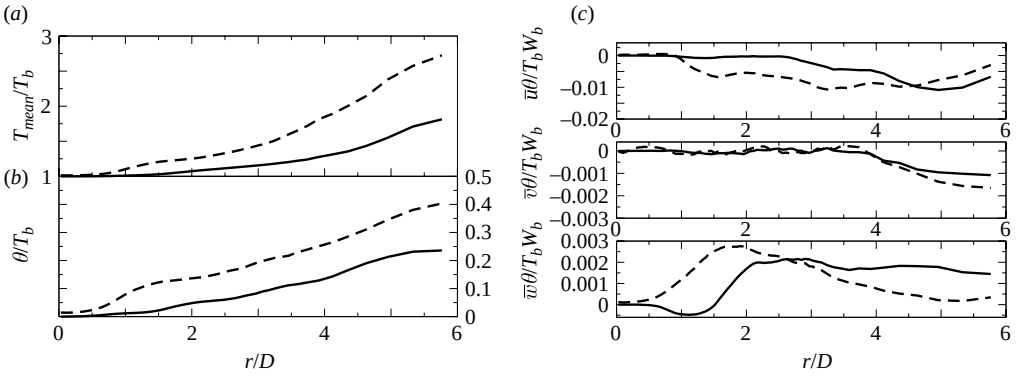

FIGURE 31. (*a*) Mean-temperature, (*b*) temperature variance and (*c*) the turbulent heat-flux components in the wall-parallel plane at ——, $z/D = 0.05$ and - - -, $z/D = 0.0125$.

argument that heat transfer here is enhanced by the jet flapping and the consequent oscillation of the impingement point, and partly by a strong acceleration of the fluid from the centre to the jet periphery. As a result of the flow impingement, the boundary layer in the stagnation point is very thin. This enables efficient heat transport from the impingement wall. In contrast, the Nusselt number seems to be closely correlated with the turbulence kinetic energy around and beyond the second Nusselt-number maximum: the peak in the kinetic energy appears approximately at the same position as the second *Nu* peak predicted by the LES. Recall that this is the region of formation of strong near-wall eddy structures originating from the breakdown of the wall-attached separation bubbles, which explains the enhanced production and level of turbulence energy. Since these eddies roll up on the wall surface, they are able to penetrate deep into the boundary layer, increasing the shear stress and heat transfer. After the wall-jet is formed, the Nusselt number continues to decrease steadily. Although the two maxima in the radial distribution of the Nusselt number are caused by different mechanisms, the major role in their formation is played by the dynamics of the large-scale vortex structures created in the jet shear layer. This can also be concluded from figure 26(*a*), where the highest amplitudes in the oscillations of the instantaneous Nusselt number occur in the stagnation region and in the region around the second maximum.

The mean properties and the second moments of the temperature field at the same wall-parallel planes at $z/D = 0.0125$ and 0.05 as the velocity field are shown in figure 31. The mean temperature (figure 31*a*) shows a smooth and monotonic increase in the radial direction in congruence with the monotonic radial decrease in the Nusselt number, but without pronounced double minima that would correspond to the double peaks in the Nusselt number. The same can be concluded for the temperature variance, as shown in figure 31(*b*). However, for $z/D = 0.0125$, both variables show mild, but visible kinks around the Nusselt number dip, which fade away with an increase in the wall distance (compare with e.g. $z/D = 0.05$). The temperature–velocity correlation is illustrated in figure 31(*c*) which shows the components of the turbulent heat flux vector $\overline{\theta u_i}$. Admittedly, the two cross-sections at which these profiles are shown ($z/D = 0.0125$ and 0.05) may not be sufficiently informative of the turbulent heat flux field, but the results presented in figure 31 are reasonably indicative. As expected, the heat flux components in the wall-parallel directions are very small in the stagnation region and increase in the radial direction while remaining negative. In particular,

the azimuthal component $\overline{\theta v}$ remains almost zero at both wall distances considered all the way up to $r/D \approx 4.0$, when it starts to increase monotonically. The radial component $\overline{\theta u}$ follows the same pattern, remaining negligible at both planes up to $r/D = 1.0$, when it begins to increase, especially at $z/D = 0.0125$. Comparison with the mean temperature distribution shows that $\overline{\theta u}$ seems to follow the simple (isotropic) eddy diffusivity concept, i.e. $\overline{\theta u} \propto -\partial T/\partial r$, but only qualitatively. The wall-normal component follows the distribution of the kinetic energy, exhibiting a peak at roughly the same position $r/D = 1.8$ in the plane $z/D = 0.0125$, which is close to the location of the second Nusselt-number maximum. While no clear relationship with the Nusselt number can be established in the stagnation region, for larger radial distances for $r/D > 2.0$ the wall-normal heat flux very close to the wall (at $z/D = 0.0125$) reflects the Nusselt-number distribution, substantiating again the conjecture that in the wall-jet region the heat transfer complies with the common boundary-layer concept. Admittedly, the molecular flux (conduction) here is of the same order of magnitude.

It is recalled, however, that the dynamics of the turbulent heat flux, as can be inferred from its full transport equation, is governed both by the mean temperature gradient and the mean rate of strain, interacting with the turbulent stress and turbulent heat flux, respectively, and is much influenced by the convection and turbulent diffusion, especially in the stagnation region.

Because our primary focus here is the vortical structures and their thermal imprint on the impinging wall, more detailed discussion of the Reynolds-averaged properties is beyond the scope of this paper and it is left for a future publication.

6. Conclusions

LES simulations of a turbulent round jet issuing from a fully developed pipe flow at $Re = 20\,000$ and impinging normally on a hot plane surface at the nozzle-to-plate-distance $H/D = 2$, provided detailed four-dimensional information on the fluid flow and heat transfer. The results – some inaccessible to experiments – were used to study the velocity, temperature and turbulence fields, dynamics of coherent vortical structures, their relationship to the thermal field, and their thermal signature on the impingement wall. Prior to the analysis, results were verified by comparison with the available experimental data.

The analysis of the three main jet zones through which the fluid passes (the free jet, the stagnation region and the radial wall jet) although mutually dependent, each show a distinct dynamics with a number of specific features. The dominant event that governs the flow and heat transfer are the roll-up vortices, generated by instabilities in the initial shear layer. The Strouhal number, which defines the natural frequency of the ring-vortex production, is found to be 0.64. As they travel downstream, the vortex rings stretch, become highly distorted and break up into vortical nests that act as precursors of the coherent turbulence eddy structure. The imprints of these large structures on the impinged wall do not form closed circles. This means that the large-scale structures in the bulk of the impingement zone and at the moment when they impact the wall, are neither circular not parallel to the target wall, but tilted and broken into segments. Occasionally a ring vortex retains its identity until the impact. The specific dynamics of the thermal field and the wall heat transfer for the present configuration are reflected in a non monotonic, double-peaked Nusselt-number distribution.

Further from the jet centre, the iso-surface of the instantaneous pressure field reveals again a large toroidal-vortex structure, generated at the edge of the radial

wall jet. The shape and size of these structures suggest that they are linked to and affected by the large-scale structures from the free jet shear layer, which survive the impingement and become deflected radially by an accelerating stream of fluid. The radial flow spreading leads to vortex stretching in the azimuthal direction which enhances their rotation. As a result, the counter-rotating vortices are formed very close to the wall. These wall-attached eddies, appearing as recirculation bubbles are further stretched before they are destroyed and entrained into the turbulent wall-jet. The presence of these eddies increases the turbulence level in this region.

Despite detailed exploration using the Q-criterion as vortex identifiers, no organized eddy structures were observed in the stagnation region around the jet centre. However, the near-wall streaks are observed in the wall-jet region. Owing to the radial flow spreading, a single streak occasionally branches into two separate streaks. It is also observed that two streaks occasionally merge into one larger streak, mainly at the locations where the wall-jet strongly decelerates. However, the mechanism behind the streak merging remains unclear.

The Nusselt-number distribution in the jet configuration considered, is characterized by two local maxima and a dip between them. The highest value of the Nusselt number occurs in the centre of the stagnation region. The local maximum of the turbulence kinetic energy at this station (figure 13*b*) is almost three times smaller than the maximum turbulence energy in a corresponding pipe flow (figure 7*a*). This indicates that the maximum Nusselt number cannot be the consequence of turbulence, but rather of the strong jet flapping and precessing (figure 21).

The specific conclusions emerging from the above observations can be summarized as follows.

(i) The roll-up vortices formed at the edge of the free jet are short-lived and undergo a faster stretching, deformation and breakdown than in a free jet because of the jet radial deflection and spreading caused by the impinged wall. Prior to their breakdown, the roll-up ring vortices become tilted with respect to the impinged plate.

(ii) The remnants of the original roll-up vortices with high vorticity concentration ('vortical nests') form large-scale eddy structures, which impinge on the wall periodically with a frequency close to that of the roll-up vortex formation. This asymmetric and periodic impingement, together with the pressure pulsations due to periodic jet shrinking and expanding associated with the formation of ring vortices, leads to jet flapping and precessing, which is believed to be instrumental in the surface renewing and enhanced heat transfer in the stagnation region.

(iii) As a consequence of the jet flapping, the stagnation point meanders in time around the jet geometrical centre, branching occasionally into two stagnation points/regions, or forming also a stagnation line.

(iv) The above conjecture on the dominant role of the periodic impact of large-scale eddies on the wall heat transfer is also substantiated by the low level of stochastic turbulence and even negative production of the time-averaged turbulence kinetic energy around the stagnation point.

(v) The instantaneous Nusselt number follows the distribution pattern of the wall friction factor – apart, of course, in the stagnation point and around – but the variations are not conclusively in phase, showing both the full in-phase and out-of-phase instantaneous behaviour.

(vi) The dip between the two peaks in the Nusselt number is the consequence of the local periodic separation on the wall and the consequent thickening of the thermal boundary layer; the recirculating fluid becomes trapped and heated, reducing thus its heat removal capacity.

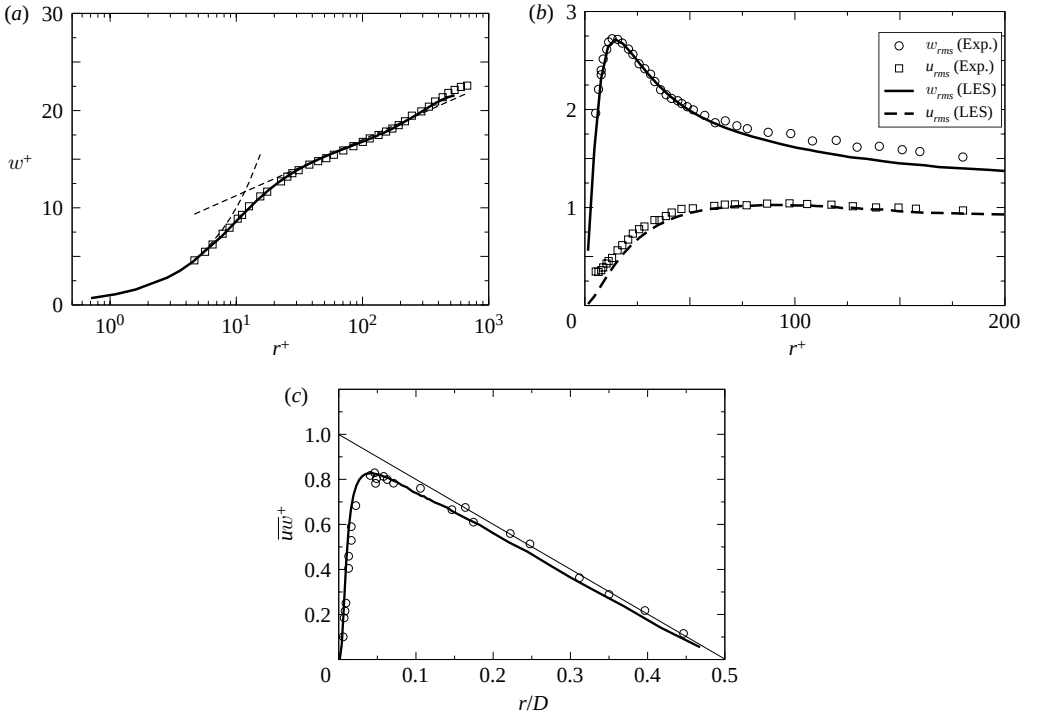

FIGURE 32. LES of a pipe flow. (*a*) Mean-velocity profile: solid line, LES; dash line, log-law; symbols, experiments of Toonder & Nieuwstadt (1997) $Re = 24\,600$. (*b*) Resolved-axial and -radial profiles of r.m.s. of the normal stresses: line, LES; symbols, experiments of Toonder & Nieuwstadt (1997) $Re = 17\,800$. (*c*) Resolved shear stress: solid line, LES; symbols, experiments of Toonder & Nieuwstadt (1997) $Re = 24\,600$.

(vii) The second peak in the Nusselt number, pertinent only for small H/D and high Re numbers, is believed to be caused by reattachment of the recirculation bubble and associated turbulence production, as well as subsequent strong advection.

We note at the end that irrespective of the subgrid-scale model used, large-eddy simulations of impinging flows require a careful grid resolution in the near-wall region in order to capture properly the near-wall turbulence dynamics and the related heat transfer. Equally important is the fine resolution of the shear layer in the initial zone of the free jet, which appeared to be crucial for the proper resolving of the initial instabilities and the formation of roll-up vortices.

The use of unstructured grid makes it possible to rationalize the total number of grid cells and improve the computational economy. However, it should be admitted that unstructured grids with non-hexahedral cells, especially when using energy-non-conserving discretization schemes, involve increased uncertainties with regard to accuracy and fidelity of LES. The great sensitivity of the computed results to the mesh resolution and quality, experienced in this work, illustrates that LES of complex flows, especially when using unstructured grids, require careful scrutiny before we can have full confidence in the results.

M.H. acknowledges the financial support of the Faculty for Applied Sciences of the Delft University of Technology, Netherlands. The simulations were conducted

on SARA (Computing and Networking Services) supercomputer TERAS installed in Amsterdam, The Netherlands.

Appendix. LES of a turbulent pipe flow

The LES simulation of the turbulent pipe flow was performed in order to generate the inflow conditions for the LES simulation of the impinging-jet flow. The hybrid mesh was used with hexahedral cells near the wall and the tetrahedral prisms in the core region with $\Delta z^+ = 33$, $\Delta r^+ = 0.7$ and $r\Delta\theta^+ = 9.7$ at the wall. The velocity components in the axial (z), radial (r) and azimuthal (θ) directions are denoted by W, U and V. The simulation results are shown in figure 32.

REFERENCES

Ashforth-Frost, S. & Jambunathan, K. 1996*a* Effect of nozzle geometry and semi-confinement on the potential core of a turbulent axisymmetric free jet. *Intl Commun Heat Mass Transfer* **23**, 155–162.

Ashforth-Frost, S. & Jambunathan, K. 1996*b* Numerical prediction of semi-confined jet impingement and comparison with experimental data. *Intl J. Numer. Meth. Fluids* **23**, 295–306.

Baughn, J. W. & Shimizu, S. 1989 Heat transfer measurement from a surface with uniform heat flux and an impinging jet. *Trans. ASME* C: *J. Heat Transfer* **111**, 1096.

Beaubert, F. & Viazzo, S. 2003 Large eddy simulations of plane turbulent impinging jets at moderate Reynolds numbers. *Intl J. Heat Fluid Flow* **24**, 512–519.

Behnia, M., Parneix, S., Shabany, Y. & Durbin, P. A. 1999 Numerical study of turbulent heat transfer in confined and unconfined impinging jets. *Intl J. Heat Mass Transfer* **20**, 1–9.

Chung, Y. M. & Luo, K. H. 2002 Unsteady heat transfer analysis of an impinging jet. *Trans. ASME* C: *J. Heat Transfer* **124**, 1039–1048.

Colucci, D. & Viskanta, R. 1996 Effect of nozzle geometry on local convective heat transfer to a confined impinging air jet. *Expl Thermal Fluid Sci.* **13**, 71–80.

Cooper, D., Jackson, D. C., Launder, B. E. & Liao, G. X. 1993 Impinging jet studies for turbulence model assessment-i. flow field experiments. *Intl J. Heat Fluid Flow* **36**, 2675–2684.

Fröhlich, J. & Rodi, W. 2002 Introduction to large-eddy simulation of turbulent flows. In *Closure Strategies for Turbulent and Transitional Flows* (ed. B. E. Launder & N. D. Sandham), pp. 267–298. Cambridge University Press.

Geers, L., Hanjalić, K. & Tummers, M. 2004 Experimental investigation of impinging jet arrays. *Exps. Fluids* **36**, 946–958.

Geers, L., Tummers, M. & Hanjalić, K. 2005 PIV-based identification of coherent structures in normally impinging multiple jet. *Phys. Fluids* **17**, 055105:1–13.

Geers, L., Hanjalić, K. & Tummers, M. 2006 Wall imprint of turbulent structures and heat transfer in multiple impinging jet arrays. *J. Fluid Mech.* **546**, 255–284.

Germano, M., Piomelli, U., Moin, P. & Cabot, W. H. 1991 A dynamic subgrid-scale eddy viscosity model. *Phys. Fluids* A **3**, 1760–1765.

Hadžiabdić, M. 2006 LES of flow and heat transfer in a round impinging jet. PhD thesis, Delft University of Technology, Delft, The Netherlands.

Han, B & Goldstein, R. J. 2003 Instantaneous energy separation in a free jet. Part i. Flow measurement and visualization. *Intl J. Heat Mass Transfer* **46**, 3975–3981.

Hanjalić, K., Popovac, M. & Hadžiabdić, M. 2004 A robust near-wall elliptic relaxation eddy-viscosity turbulence model for CFD. *Intl J. Heat Fluid Flow* **25**, 1047–1051.

Hattori, H. & Nagano, Y. 2004 Direct numerical simulation of turbulent heat transfer in plane impinging jet. *Intl J. Heat Fluid Flow* **25**, 749–758.

Kataoka, K. 1990 Impingement heat transfer augmentation due to large scale eddies. In *Heat Transfer 1990, Proc. 9th Intl Heat Transfer Conf.* vol. 1, pp. 255–273.

Lee, J. & Lee, S. J. 2000 The effect of nozzle configuration on stagnation region heat transfer enhancement of axisymmetric jet impingement. *Intl J. Heat Mass Transfer* **43**, 3497–3509.

Leonard, B. P. 1979 A stable and accurate convective modelling procedure based on quadratic upstream interpolation. *Comput Meth. Appl. Mech. Engng* **19**, 59–98.

Leonard, B. P. 1988 Simple high-accuracy resolution program for convective modelling of discontinuities. *Intl J. Numer Meth. Fluids* **8**, 1291–1318.

Livingood, J. N. B. & Hrycak, P. 1973 Impingement heat transfer from turbulent air jets to flat plates – a literature survey. *NASA TM* X–2778.

Lytle, D. & Webb, B. 1994 Air jet impingement heat transfer at low nozzle-plate spacings. *Intl J. Heat Mass Transfer* **37**, 1687–1697.

Lytle, D. & Webb, B. W. 1991 Secondary heat transfer maxima for air jet impingement at low nozzle-to-plate spacing. In *Experimental Heat Transfer, Fluid Mechanics and Thermodynamics* (ed. J. F. Keffer, R. K. Shah & E. N. Ganic). Elsevier.

Nishino, K., Samada, M., Kasuya, K. & Torii, K. 1996 Turbulence statistics in the stagnation region of an axisymmetric impinging jet flow. *Intl J. Heat Fluid Flow* **17**, 93–201.

Ničeno, B. 2001 An unstructured parallel algorithm for large eddy and conjugate heat transfer simulations. PhD thesis, Delft University of Technology, Delft, The Netherlands.

Ničeno, B. & Hanjalić, K. 2004 Unstructured large-eddy and conjugate heat transfer simulations of wall-bounded flows. In *Modeling and Simulation of Turbulent Heat Transfer (Developments in Heat Transfer Series)* (ed. M. Faghri & B. Sunden). WIT Press.

Olsson, M. & Fuchs, L. 1998 Large eddy simulation of a forced semiconfined circular impinging jet. *Phys Fluids* **10**, 476–486.

Pauley, L. R., Moin, P. & Reynolds, W. C. 1990 The structure of two-dimensional separation. *J. Fluid Mech.* **220**, 397–411.

Piomelli, U. & Chasnov, J. R. 1996 Large-eddy simulations: theory and applications. In *Transition and Turbulence Modelling* (ed. A. Henningson, K. Hallback, L. Alfredsson & M. Johansson). Kluwer.

Pope, S. B. 2000 *Turbulent Flows*. Cambridge University Press.

Popiel, C. O. & Trass, O. 1991 Visualization of a free and impinging round jet. *Expl Thermal Fluid Sci.* **4**, 253–264.

den Toonder, J. M. J. & Nieuwstadt, F. T. M. 1997 Reynolds number effects in a turbulent pipe flow for low to moderate *Re*. *Phys. Fluids* **9**, 3398–3409.

Tsubokura, M., Kobayashi, T., Taniguchi, N. & Jones, W. P. 2003 A numerical study on the eddy structures of impinging jets excited at the inlet. *Intl J. Heat Fluid Flow* **24**, 500–511.

Viskanta, R. 1993 Heat transfer to impinging isothermal gas and flame jets. *Expl Thermal Fluid Sci.* **6**, 111–134.

Voke, P. R. & Gao, S. 1998 Numerical study of heat transfer from an impinging jet. *Intl J. Heat Mass Transfer* **41**, 671–680.

Yan, X. & Saniei, N. 1997 Heat transfer from an obliquely impinging circular air jet to a flat plate. *Intl J. Heat Fluid Flow* **18**, 591–599.

Yule, A. J. 1978 Large-scale structure in the mixing layer of a round jet. *J. Fluid Mech.* **3**, 413–432.